

ORIGINAL ARTICLE

Coupling non-invasive imaging and reactive transport modeling to investigate water and oxygen dynamics in the root zone

Sarah Bereswill¹  | Hannah Gatz-Miller²  | Danyang Su²  | Christian Tötze^{1,3}  |
Nikolay Kardjilov³  | Sascha E. Oswald¹  | Klaus Ulrich Mayer² 

¹Institute of Environmental Science and Geography, University of Potsdam, Potsdam, Germany

²Department of Earth, Ocean and Atmospheric Sciences, The University of British Columbia, Vancouver, British Columbia, Canada

³Institute of Applied Materials, Helmholtz Centre Berlin for Energy and Materials, Berlin, Germany

Correspondence

Sarah Bereswill, Institute of Environmental Science and Geography, University of Potsdam, Karl-Liebknecht-Str. 24–25, 14476 Potsdam, Germany.
Email: bereswill@uni-potsdam.de

Assigned to Associate Editor Christophe Darnault.

Funding information

Deutsche Forschungsgemeinschaft, Grant/Award Numbers: OS 351/8-1, TO 949/2-1, project no. 396368046; Deutsche Forschungsgemeinschaft (DFG, German Research Foundation), Grant/Award Number: 491466077

Abstract

Oxygen (O₂) availability in soils is vital for plant growth and productivity. The transport and consumption of O₂ in the root zone is closely linked to soil moisture content, the spatial distribution of roots, as well as structure and heterogeneity of the surrounding soil. In this study, we measure three-dimensional root system architecture and the spatiotemporal dynamics of soil moisture (θ) and O₂ concentrations in the root zone of maize (*Zea mays*) via non-invasive imaging, and then construct and parameterize a reactive transport model based on the experimental data. The combination of three non-invasive imaging methods allowed for a direct comparison of simulation results with observations at high spatial and temporal resolution. In three different modeling scenarios, we investigated how the results obtained for different levels of conceptual complexity in the model were able to match measured θ and O₂ concentration patterns. We found that the modeling scenario that considers heterogeneous soil structure and spatial variability of hydraulic parameters (permeability, porosity, and van Genuchten α and n), better reproduced the measured θ and O₂ patterns relative to a simple model with a homogenous soil domain. The results from our combined imaging and modeling analysis reveal that experimental O₂ and water dynamics can be reproduced quantitatively in a reactive transport model, and that O₂ and water dynamics are best characterized when conditions unique to the specific system beyond the distribution of roots, such as soil structure and its effect on water saturation and macroscopic gas transport pathways, are considered.

1 | INTRODUCTION

The availability of oxygen in soils is of critical importance for plant growth and agricultural productivity, as it affects the development and physiological functioning of root

systems (Ben-Noah & Friedman, 2018). Roots require O₂ for aerobic respiration, supplying energy for tissue growth and maintenance, as well as water and nutrient uptake (Armstrong & Drew, 2002; Lambers et al., 2013). Commonly, diffusion in soil gas is the principal mode of transport of O₂ to roots, although advective gas transport can contribute to soil aeration in certain cases (Ben-Noah & Friedman, 2018). In unsaturated soils, the gas-filled pore space forms the main transport path for O₂, as diffusion of O₂ is four orders of

Abbreviations: 2D, two-dimensional; 3D, three-dimensional; NCL, neutron computed laminography; RSA, root surface architecture; RSD, root surface density (m² root surface area m⁻³ bulk soil); RT, reactive transport; RWU, root water uptake; VG, Van Genuchten.

This is an open access article under the terms of the [Creative Commons Attribution-NonCommercial-NoDerivs](https://creativecommons.org/licenses/by-nc-nd/4.0/) License, which permits use and distribution in any medium, provided the original work is properly cited, the use is non-commercial and no modifications or adaptations are made.

© 2023 The Authors. *Vadose Zone Journal* published by Wiley Periodicals LLC on behalf of Soil Science Society of America.

magnitude faster in air compared to water (Neira et al., 2015). Consequently, soil moisture content and its spatial variation affect diffusive transport of O_2 toward the roots (Cook et al., 2013) by altering air-filled porosity and therefore the air-filled pores' connectivity and tortuosity (Masís-Meléndez et al., 2015). Local differences in soil physical properties such as porosity, permeability, bulk density, soil moisture retention, macropore abundance, and connectivity, as well as macroscale structural features such as cracks, can further impact gas transport (Ben-Noah & Friedman, 2018; Hamamoto et al., 2009; Katuwal et al., 2015). Along with spatiotemporal variation in root respiration rates and microbial O_2 demand, these heterogeneous conditions pose challenges to the measurement and modeling of O_2 transport dynamics in unsaturated soils, and raise the question of how to best account for local heterogeneity in models (Vereecken et al., 2016).

Noninvasive imaging techniques enable high-resolution and spatiotemporally resolved monitoring of the distribution of soil moisture and root water uptake (RWU) (Tötze et al., 2021; Zarebanadkouki et al., 2013), as well as the concentration patterns of gases and solutes, including exudates, in the rhizosphere (Blossfeld et al., 2013; Holz et al., 2019). Experiments combining neutron imaging and planar optodes have shown that the O_2 concentration in the root zone is closely related to the local water content (Rudolph-Mohr et al., 2021, 2017). A critical next step to understand the transport, uptake, and reaction processes taking place in the root zone in more detail, is to use data gained from high resolution imaging experiments for the set-up, calibration, and validation of numerical models (Roose et al., 2016).

Reactive transport (RT) models, such as MIN3P (Mayer et al., 2002, 2012), are a type of numerical model particularly suitable for investigating complex processes in rooted soils because they couple the flow of water and the transport of gases and solutes in the saturated and unsaturated zone with a network of biogeochemical reactions (Li et al., 2017; Nowack et al., 2006). Specific to plant-soil interactions, MIN3P has been used to study, for example, silicon cycling in forested soils (Gérard et al., 2008), the impact of variation in RWU on nutrient availability (Espeleta et al., 2017), nickel concentrations in the rhizosphere (Moradi et al., 2010), and the oxalate-carbonate pathway of the Iroko tree (Gatz-Miller et al., 2022), but has not yet been used to characterize the transport of O_2 in the root zone as a function of soil moisture and other root processes. As noninvasive imaging is also capable of providing in-situ high-resolution data on the root system architecture (RSA), combining imaging and RT modeling yields a new opportunity to analyze root behavior in relation to soil geochemistry in directly observed experimental systems at high spatial and temporal resolution.

A key question in numerical modeling of soil-root interactions revolves around the degree to which complexity in numerical models is needed to representatively characterize

Core Ideas

- Root system architecture, soil moisture (θ), and oxygen (O_2) concentrations were measured via non-invasive imaging.
- A reactive transport model was parameterized for process-based analysis of spatiotemporal θ and O_2 concentration evolution.
- Considering spatial heterogeneity in soil hydraulic parameters was key to reproduce measured θ and O_2 distribution.

soil-plant systems, and where complexity may be unnecessary. In this study, we addressed the spatiotemporal dynamics of soil moisture and O_2 concentration in the root zone of maize (*Zea mays*) by obtaining three-dimensional (3D) root information via neutron computed laminography (Rudolph-Mohr et al., 2021) and, in a time-lapse two-dimensional (2D) imaging set-up of neutron radiography combined with optode imaging, simultaneously capturing changes in soil moisture distribution and soil O_2 , and then used these data to construct and parameterize an RT model of the experimental system. The combination of three different noninvasive imaging techniques (neutron computed laminography, neutron radiography, and optode imaging) together with RT modeling, allowed for comparison between quantitative model output and real data of a 3D root-soil sample, representing a novel approach to mapping water content and O_2 dynamics of soil with a living root system.

The overarching objective of this study is to explore the role of spatially distributed RWU and respiration, as well as structure and heterogeneity of the bulk soil on the distribution and evolution of soil water content and O_2 concentrations, and to assess the necessity for inclusion of soil heterogeneity and complexity when modeling root-soil interactions. Specifically, the aims of this study are (i) to parameterize a soil-plant focused RT model with results from the imaging experiment at the plant-scale and, (ii) to explore the role of heterogeneity of bulk soil physical characteristics with regard to the observed changes in soil moisture content and O_2 concentrations. To this end, we compared three different simulation scenarios as follows: (i) homogeneous hydraulic properties throughout the soil domain; (ii) presence of macroscopic crack structures; (iii) local variation of permeability and porosity, in combination with subsequent variation in soil moisture retention via inclusion of spatial heterogeneity of van Genuchten (VG) parameters α and n (van Genuchten, 1980).

Due to the nature of this work, in which we first conduct the experiments and then construct models based on the

experimental results, we first describe experimental set-up and results, followed by the modeling approach and results, before moving on to general discussion of imaging and modeling results in tandem.

2 | EXPERIMENT

2.1 | Plant imaging experiment set-up

2.1.1 | Rhizotron preparation and plant growth

We prepared six boron-free glass rhizotrons (inner dimensions $0.142 \text{ m} \times 0.15 \text{ m} \times 0.015 \text{ m}$) for the plant imaging experiment. First, we glued one in-house manufactured O_2 optode ($0.12 \text{ m} \times 0.11 \text{ m}$; see Rudolph-Mohr et al. (2014) for further detail) to the inner front window of each rhizotron. Optode calibration was conducted with a small optode replicate in a separate glass box filled with soil using water containing O_2 concentrations between 0 mg L^{-1} and 10 mg L^{-1} (see Rudolph-Mohr et al., 2014). A second calibration was conducted by flushing a glass box, equipped with an optode replicate and filled with soil, with nitrogen gas ($0\% \text{ O}_2$), air ($21\% \text{ O}_2$), and pure O_2 gas at 21°C . Sandy soil collected at the artificial catchment “Chicken Creek” in Cottbus, Germany (91% sand, 8% silt, 1% clay, $\text{pH}_{(\text{CaCl}_2)}$ 7.6, total carbon 0.13%, total nitrogen (N) 0.01%, CAL-P 8.6 mg kg^{-1} , mean dry bulk density 1.42 g cm^{-3}) was first sieved to $<2 \text{ mm}$ and then filled into the rhizotrons to a height of 0.085 m. Subsequently, a 0.01 m wide horizontal layer of quartz powder (Microsil M 4, Euroquarz GmbH, Dorsten Germany; average particle size 0.051 mm, 27% sand, 58% silt, and 15% clay) was placed on top of the soil layer, and then more soil was subsequently added on top (to 0.11 m total height). The purpose of this horizontal “barrier” layer, which separated the soil domain into an upper and a lower compartment, was to restrict gas exchange of the lower compartment with the atmosphere without affecting root growth, due to its hydraulic properties (similar to clayey material). In this way, uptake and release processes of water, gas, and solutes in the lower compartment were isolated to the roots.

Six germinated maize seeds (*Zea mays* L., cultivar: Golden Bantam) were planted (one per rhizotron) and after sprouting, the soil surface was covered with a layer of washed gravel to minimize evaporation. The maize plants were grown in a plant growth chamber located at the Institute of Environmental Science and Geography at the University of Potsdam. They were illuminated with light intensity of $400 \mu\text{mol m}^{-2} \text{ s}^{-1}$ between 6 a.m. and 8 p.m., at $23/19^\circ\text{C}$ day/night temperature and a constant relative humidity of 60% and irrigated every second day with the amount of water required to maintain the volumetric soil moisture content (θ) between 0.20 and $0.25 \text{ m}^3 \text{ m}^{-3}$. Nutrient solution (7% N, 3% P_2O_5 , 6% K_2O , and micronutrients, details in Rudolph-Mohr et al., 2017) was applied twice

per week. Three small holes at the bottom of the rhizotron allowed for drainage of excess water, as well as irrigation from the bottom. Irrigation was stopped 2 days before plants were transferred to the neutron imaging facility (plant age 13 days). The rhizotron set-up is illustrated in Figure 1a.

2.1.2 | Imaging experiment

From the six maize plants, three individuals with a well-developed root system were chosen for the imaging experiment. We measured RSA and the evolution of soil moisture content and O_2 concentration in the rhizosphere of maize via a combination of three different imaging techniques as follows: 3D neutron computed laminography (NCL; measurement of RSA and position of roots within the rhizotron), 2D neutron radiography (soil moisture content), and 2D optode imaging (O_2 concentration). First, we applied NCL at low soil moisture content ($\theta = 0.08 \pm 0.01$) to obtain high contrast between roots and soil facilitating segmentation of roots. Afterwards, we watered the rhizotrons from the bottom via capillary rise by placing them in a container filled with water (water table at 0.09 m) for 30 min (“rewetting”). Finally, the rhizotrons were weighed and then sealed at the bottom with aluminum tape to prevent further water and gas exchange at the base.

One hour after rewetting ($t = 1 \text{ h}$), we measured O_2 concentration and soil moisture distribution via 2D optode imaging and neutron radiography. This imaging procedure was repeated every 2–3 h until 52 h after watering. The rhizotrons were also weighed repeatedly to monitor water loss during the 52 h observation period. As no further irrigation took place and evaporation was assumed negligible due to the gravel layer on the soil surface, water loss was attributed to transpiration only and was later used as a basis for estimation of an average water loss flux in the model simulations.

The imaging experiments were performed at the BERII research reactor at the Helmholtz Centre Berlin for Energy and Materials using the CONRAD-2 instrument (Kardjilov et al., 2016). NCL is a modified tomographic approach for 3D imaging of flat objects. Tilting the rotational axis of the sample reduces artefacts caused by insufficient neutron transmission through the laterally extended side of the sample (Helfen et al., 2011). In a previous experiment, we demonstrated the capability of NCL to study root systems grown in slab-shaped rhizotrons and successfully tested the combination of NCL with 2D optode imaging (Rudolph-Mohr et al., 2021). To image the RSA of the maize plants in 3D, we captured 600 projection images over an angular range of 300° , as well as 15 flat-field and 15 dark-field images, each with exposure time of 15 s, resulting in total acquisition time of approximately 4 h for NCL. The optode imaging equipment consisted of a cooled CCD camera system with a 500 nm long-pass filter and a separate UV light source and was set up inside the measurement hut next to the neutron detector system. An automated

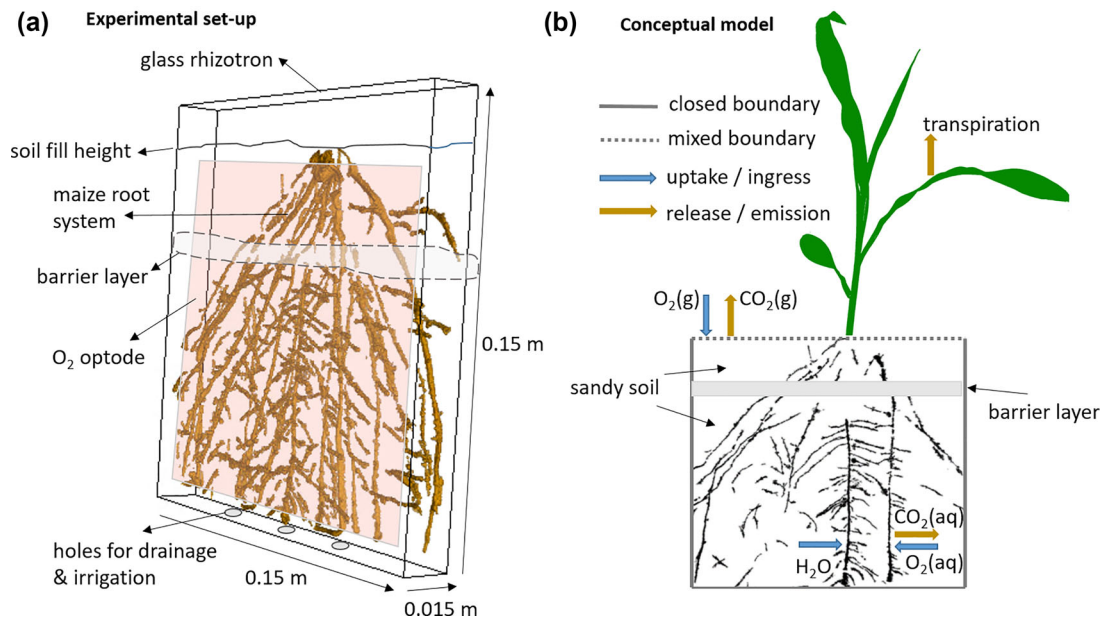


FIGURE 1 (a) Illustration of the rhizotron system with O_2 optode (light pink area) and the maize root system (3D rendering from segmented dataset of 3D neutron computed laminography). The rhizotron was filled with sandy soil up to a height of 0.11 m; a horizontal layer of quartz powder with hydraulic properties similar to a silty clay acted as a “barrier” for diffusive gas transport, but did not restrict root growth. (b) Conceptual model of the sinks and sources in the experiment. Simulated processes were: exchange of O_2 and CO_2 between soil and atmosphere at the upper rhizotron boundary, transpiration by the maize plant (evaporation was neglected because of the gravel layer located on top of the soil surface), root water uptake, root respiration (uptake of O_2 and release of CO_2). Uptake or inflow is illustrated with blue, release or emission with yellow arrows. The sides and the base of the rhizotron were simulated as no-flow boundaries, while the upper boundary allowed for gas exchange with the atmosphere. aq, aqueous phase; g, gaseous phase.

system translated the sample into the neutron beam for radiography immediately after optode imaging. Plants were in the neutron instrument only during imaging; between the measurements, they were kept in a plant growth chamber near the neutron instrument (under the same conditions as during the growth period). The nominal spatial resolution of the measurement was $127 \mu\text{m}/\text{voxel}$ (NCL), $127 \mu\text{m}/\text{pixel}$ (neutron radiography), and $196 \mu\text{m}/\text{pixel}$ (optode imaging). More details on spatial and temporal resolution of the three imaging modalities can be found in the Supporting Information Section S1.

2.1.3 | Image post-processing and co-registration

Neutron images from both NCL and radiography (Figure 2) were corrected for camera noise and beam fluctuations applying a darkfield-flatfield correction (as described in Oswald et al., 2008) and the projections from NCL were reconstructed to a 3D volume (Octopus Reconstruction 8.9.4, Inside Matters, Gent/Belgium; cone beam geometry, axis skew: 20°). To reduce noise in the neutron radiographs and optode images, the median of five images per time step was calculated in ImageJ (Schneider et al., 2012) for further analysis. Image

time series of moisture content and O_2 concentration were first registered separately to correct for deviations of sample orientation respective to the camera or the scintillator perspective (ImageJ, plugin: StackReg, transformation: rigid body, corrected manually if needed). Subsequently, the datasets from the three different image modalities were co-registered to spatially correlate root position, soil moisture content, and oxygen concentrations. Through scaling, field of view adjustment and the placement of multiple “anchor points” set at features such as the rhizotron boundary or the sample holder followed by pixel wise translation and rotation, precise alignment of the images from NCL, radiography, and optode imaging was achieved using the scaling, translation, rotation and reslicing functions in the software ImageJ (similar to the procedure described in Haber-Pohlmeier et al., 2019). Final pixel size of the co-registered image stacks was $196 \mu\text{m}$.

2.1.4 | Root segmentation and calculation of moisture content and O_2 concentration

To extract the root system from the 3D tomogram reconstructed from the NCL scans (Figure 2a), we conducted a semiautomated segmentation, applying a region-growing

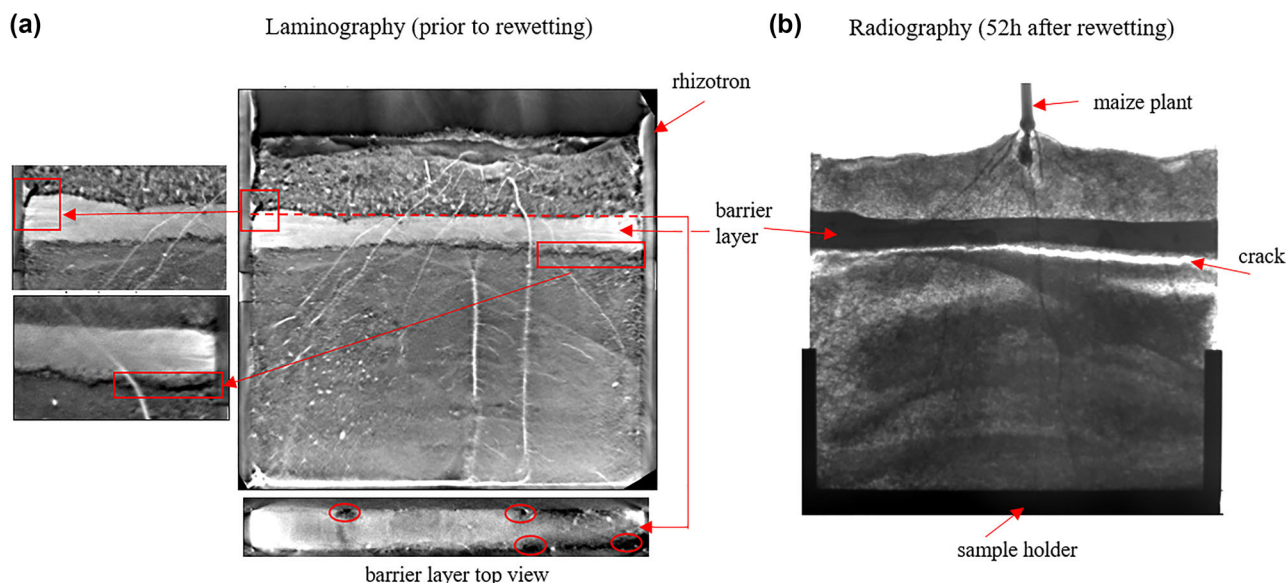


FIGURE 2 The studied system, a maize plant grown in a rhizotron (inner dimensions $0.142 \times 0.15 \times 0.015$ m) was separated into a lower and an upper compartment by a horizontal barrier layer. The function of this layer, consisting of silty-clay material, was to impede gas exchange between the lower soil compartment and the atmosphere in order to study root oxygen (O_2) consumption patterns under limited O_2 supply. Prior to rewetting, the rhizotron was scanned in 3D via neutron computed laminography (NCL) (a). The 3D information revealed that the barrier layer showed several regions where it was either discontinuous or, at the interface with the glass of the rhizotron, cracks were present (as highlighted in [a]). A crack structure right below the barrier layer was also visible in the neutron radiographs (b).

algorithm in VGStudioMax 3.1 (Volume Graphics, Heidelberg / Germany). Voxels in the 3D volume are either assigned root (foreground, gray-scale value = 1) or soil (background, gray-scale value = 0) via locally adapted gray level thresholding within regions of interest around user-defined initial seed points (dynamic mode). The segmented root volume was saved as a stack of binary images and later used as the basis for calculation of root surface density (RSD) utilized for model input. Soil moisture content was calculated from neutron radiographs as described in Rudolph-Mohr et al. (2014) using neutron attenuation coefficients derived from imaging a calibration rhizotron (filled with dry soil, with optode, without plant). Oxygen concentration maps were derived by applying the calibration curve (relating fluorescence intensity and O_2 concentration) to the gray scale optode images in MATLAB R2020a (see Rudolph-Mohr et al., 2014). In this experimental set-up, soil moisture and optode calibration was only conducted for the sandy soil, but not the barrier layer material. As a result, moisture and O_2 concentration were only analyzed within the upper and lower soil compartment of the rhizotron.

We present the main experimental results in the following, because they function as a necessary basis for model set-up and modeling analysis. Additional experimental results will be introduced together with the modeling results to facilitate direct comparison.

2.2 | Experimental results: Evolution of soil moisture and O_2 concentration after rewetting

From an average soil moisture content of $\theta = 0.08 \pm 0.01$, the soil was rewetted and a time series of neutron radiographs (Figure 3a) and optode images (1–52 h after rewetting) (Figure 3b) was captured. Soil moisture content at 1 h after wetting was spatially heterogeneous and ranged between 0.27 (mean, lower compartment; maximum: 0.30) and 0.24 (mean, upper compartment) (Figure 3a). Oxygen concentrations around the roots growing near the optode were lower than in the bulk soil (Figure 3b). Since the supply of O_2 from the ambient air to the lower compartment was constrained by the wet barrier layer, mean O_2 concentration in the lower compartment declined to 2.7×10^{-5} mol L^{-1} (15 h after rewetting). In a distinct region located below the barrier layer (“oxygen reentry zone”), O_2 concentration strongly increased to 3.1×10^{-4} mol L^{-1} at 26 h after completion of rewetting. We attribute this increase to the desaturation of cracks present within the barrier layer and at the interface of the barrier layer and rhizotron glass (Figure 2a), through which O_2 could penetrate from the upper compartment, which was in exchange with the ambient air. Crack formation likely occurred from the drying–rewetting cycle, where average soil moisture was lowered (to $\theta = 0.08 \pm 0.01$ $m^3 m^{-3}$) to achieve good contrast between roots and soil in the NCL scan. Further, the barrier

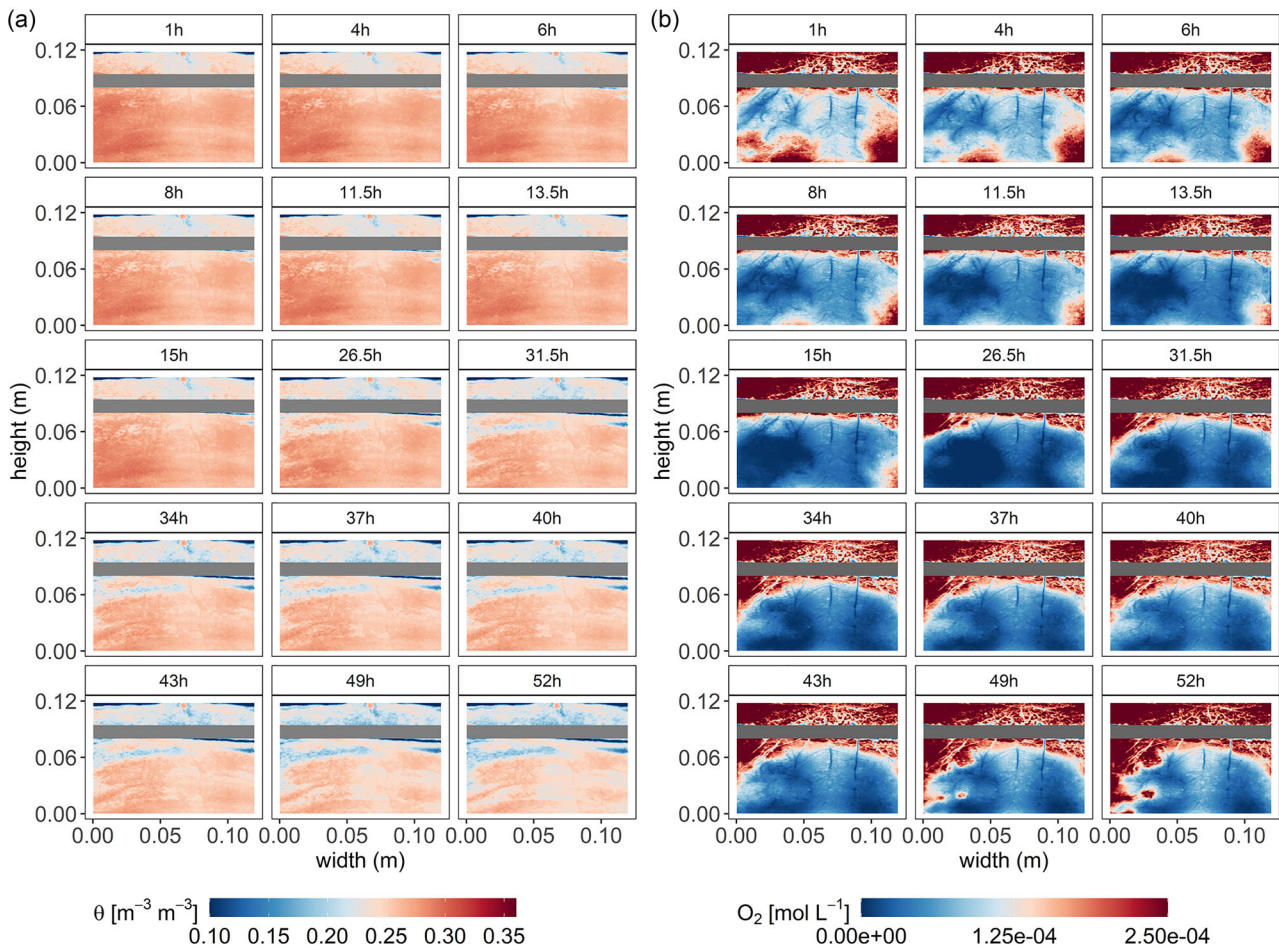


FIGURE 3 Moisture content derived from neutron radiography (a) and optode images showing oxygen (O_2) concentration (b). The time-series was captured between 1 and 52 h after rewetting the soil in the rhizotron experiment. The gray area indicates the position of the horizontal barrier layer, which separated the lower and the upper soil compartment. The clayey material in this layer (quartz powder) restricted the ingress of O_2 from the upper into the lower compartment. Calibration of both neutron attenuation (for calculation of moisture content) and O_2 optode signal was conducted only for the sandy soil, but not the clayey material used for the barrier layer (area is shaded in gray).

layer was not perfectly continuous at all places as revealed by the 3D scan (Figure 2a), implying that gas ingress could have been facilitated locally.

A zone of low O_2 concentration remained at the bottom of the rhizotron 52 h after rewetting, while the rest of the soil in the lower compartment had returned to near atmospheric O_2 levels (Figure 3b, last panel). Soil O_2 concentration in the upper compartment remained high throughout the experiment (Figure 3b), with only narrow root depletion zones, as O_2 consumed by roots could be replenished quickly from the ambient air.

3 | MODELING

The measured time-series and spatiotemporal evolution of soil moisture and O_2 concentration in the rhizotron system were reproduced and analyzed via RT modeling.

3.1 | Modeling approach

3.1.1 | Numerical model

Multicomponent reactive transport modeling is an approach that combines equations describing fluid flow, gas and solute transport simultaneously with biogeochemical reactions. Biogeochemical reactions can include kinetic processes or thermodynamically controlled processes. Reactions are typically accessed through a database that contains reaction stoichiometrics of aqueous complexation, hydrolysis, mineral dissolution-precipitation, ion exchange, surface complexation, gas exchange and redox reactions, and the associated thermodynamic parameters (Steefel et al., 2015). The geochemical system is described by a set of components (or primary unknowns) and a set of secondary species. All secondary species can be expressed in terms of the components via law of mass action relationships (Steefel et al., 2015). This

approach allows the process-based inclusion of geochemical reactions, constrained by thermodynamic relationships and data, in plant-soil interaction models, while simultaneously simulating flow and transport processes based on a physics-based formulation. The RT code used for the modeling is MIN3P, a multi-component RT code (Mayer & MacQuarrie, 2010; Mayer et al., 2002, 2012; Su et al., 2021) that considers fluid flow, solute transport, and gas transport through porous media, along with biochemical reactions involving solutes, gases, and minerals (Mayer et al., 2002, 2012; Steefel et al., 2005). MIN3P uses well-known flow, transport, and geochemical equations (e.g., Darcy's Law, Richards' equation, the advection–dispersion equation, van Genuchten soil hydraulic function relationships, law of mass action relationships and kinetic rate expressions), to simultaneously consider nonlinear and interrelated processes, such as fluid flow, solute and gas transport, gas dissolution and exsolution, adsorption, mineral dissolution and precipitation, oxidation–reduction reactions, and acid–base reactions (Mayer & MacQuarrie, 2010; Mayer et al., 2002; Mayer et al., 2015; Steefel et al., 2015; Su et al., 2021). MIN3P has recently been used for the study of soil processes in the presence of plants and soil organic matter (Gatz-Miller et al., 2022; Gérard et al., 2017; Jia et al., 2021). Processes and equations relevant to the present study will be outlined in the following sections. Further detailed information regarding MIN3P's governing equations and those relating to root and plant related processes may be found in Gérard et al. (2008, 2017), Mayer et al. (2002, 2012), and Gatz-Miller et al. (2022).

3.1.2 | Base-model set-up

From the imaging experiment, we chose one maize individual to serve as our model plant and set up a 2D model based on data from the rhizotron experiment (Figure 1). For the two other plants included in the imaging experiment, the analysis and modeling described in the following was done in a similar way (results are shown in the Supplementary Information, Section S3.3). The dimensions of the model domain were based on the zone covered by the O₂ optode in the experiment, with a height of 1.23×10^{-1} m and length of 1.18×10^{-1} m. The model domain was discretized into 210×200 grid cells. Spatial resolution for all simulations was 3.46×10^{-7} m² per grid cell, which corresponds to a 3×3 pixel binning versus the original images (pixel area 3.84×10^{-8} m²).

Per the experiment, the model domain was separated into three sections: one upper and one lower soil compartment, each consisting of sandy soil (Table 1), with the two separated by a 1.20×10^{-2} m wide low permeability barrier layer representing the quartz powder material used in the experiment (Table 1). The barrier layer was placed at an elevation between 8.16×10^{-2} m and 9.35×10^{-2} m and stretched across the

entirety of the model domain, in-line with the experimental set-up. The gravel layer present above the upper compartment in the rhizotron experiment was assumed to limit evaporation as a boundary condition, but was not otherwise included in the model. Transient simulation of water and O₂ dynamics were run for 51 h (1–52 h after rewetting the soil). The conceptual model is illustrated in Figure 1b.

3.1.3 | Bulk soil and transport parameters

The water retention curve for the sandy soil was determined in the laboratory for five replicate samples packed at bulk densities ranging from 1.33 to 1.45 g cm⁻³ (representative of values calculated from filling the rhizotrons) (Table 1). The measurements suggested an average saturated moisture content θ_s (porosity ϕ) of 0.33 (range: 0.32–0.36). As for the soil in the lower compartment itself, moisture content data (neutron radiographs) showed a maximum moisture content of 0.31 at the bottom of the lower compartment, which we assumed to represent saturation conditions at the beginning of the experiment. As a result, average porosity of the sandy material was set to 0.31 (Table 1). For the simulations accounting for material heterogeneity, porosity distribution was spatially mapped from measured moisture content and saturated hydraulic conductivity (K_{sat}). Similarly, soil hydraulic function parameters and their spatial distribution were estimated using ROSETTA (Schaap et al., 2001) and calibrated to match observed water and O₂ transport in the simulations.

For gas transport, the free phase diffusion coefficients were set to 2.0×10^{-9} m² s⁻¹ for O₂ in water (Wise & Houghton, 1966) and to 1.98×10^{-5} m² s⁻¹ in air (Schmitz et al., 2013), and we assumed a Millington tortuosity correction for water and gas diffusivity (Millington, 1959). The effects of dispersion were neglected. Temperature was set to 21°C for all simulations.

3.1.4 | Representation of the root system based on the imaging data

The RSA of the maize plant was represented in the model as a 2D distribution of local root surface density (RSD, in m² root surface m⁻³ bulk soil) per model control volume. RSD has previously been used in MIN3P RT simulations to represent the spatial distribution of roots in the modeled domain, by coupling to the root architecture software ArchiSimple, a tool to generate computerized root systems in 2D and 3D simulations (Braghiere et al., 2020; Gérard et al., 2017; Pagès et al., 2014). For this work, however, we derived RSD directly from the real RSA of the maize plant of the imaging experiment as measured via NCL, to enable as direct as possible comparison of observed O₂ patterns between the experiment and the models.

TABLE 1 Bulk soil hydraulic parameters for the sandy soil and the barrier layer material (quartz powder).

Material	Texture	θ_r	n (-)	α (m^{-1})	K_{sat} (m s^{-1})	ϕ (-)
Sandy soil	91% sand, 8% silt, 1% clay	0.04	2.7	3.1	9.80×10^{-5}	0.31
Quartz powder (barrier layer)	27% sand, 58% silt, 15% clay	0.06	1.67	0.46	2.65×10^{-6}	0.42

Note: The soil water retention curve was measured using the evaporation method (Wind method) (Iden & Durner, 2008; Peters & Durner, 2008) using a ku-pF device (UGT, Umweltgeräte Technik); the water content at a pF-value of 4.2 (or suction of 15000 hPa) was determined using a ceramic plate and pressure chamber. Saturated hydraulic conductivity (K_{sat}) was estimated based on the results of a texture analysis using Rosetta (Zhang & Schaap, 2017). Soil hydraulic parameters were then derived via optimization using the R package “SoilHyp” (Dettmann, 2022). Soil texture analysis was performed using wet sieving (sand) and laser diffraction (silt and clay fraction). Texture of the quartz powder is based on information from the manufacturer with hydraulic properties calculated using Rosetta (Schaap et al., 2001). Corresponding parameters for the crack zones in the barrier layer are provided in the Supporting Information Section S2.1. θ_r , residual volumetric moisture content ($\text{m}^3 \text{m}^{-3}$), n , van Genuchten soil hydraulic function parameter; α , Van Genuchten soil hydraulic function parameter; ϕ , porosity.

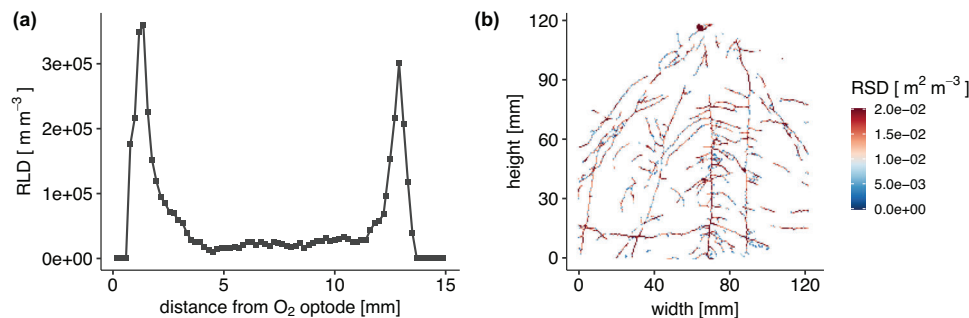


FIGURE 4 (a) Distribution of root length density (RLD) within the rhizotron relative to the distance from the oxygen (O_2) optode which was attached to the front window. The roots growing within the optode-covered area and located within 7.5 mm distance to the optode (front half of the rhizotron) were then included in the modeling study as a 2D distribution of RSD (plot b). (b) Distribution of RSD (root surface density in units of m^2 root surface m^{-3} soil) of the roots growing within 7.5 mm distance from the O_2 optode used as input for the 2D model. The 2D model was set-up for the optode covered area. Resolution versus the original neutron images is 3×3 pixels, corresponding to $3.46 \times 10^{-7} \text{ m}^2$ per model grid cell.

First, we analyzed the full 3D RSA of the maize plant and the distribution of roots within the rhizotron as obtained from the NCL scan (Figure 4a). It was found that the spatial distribution of roots was skewed toward the front and back rhizotron window (Figure 4a), with the majority of roots located on the front side within 4–5 mm distance to the O_2 optode. In a previous study, it was determined that in a similar set-up, O_2 consumption by roots in up to 7.5 mm distance to the optode (half the thickness of the rhizotron) could be detected in wet soil (Rudolph-Mohr et al., 2021). Though it is recognized that water/solute/gas from anywhere in the rhizotron could move within the detection range of the O_2 optode, we assumed that because of the bisection observed in root growth on either side of the rhizotron, water, gas, and solute present beyond 7.5 mm from the O_2 optode would more likely be drawn toward the roots on the other side of the rhizotron (Figure 4a), and so the observed moisture content and O_2 evolution was most representative of soil/water/gas within 7.5 mm of the O_2 optode. Consequently, we considered all roots located within 7.5 mm distance to the O_2 optode in our model domain.

In general, RSD refers to the surface area of the roots (S , in m^2) present in a specific soil volume (SV, in m^3). We extracted all images that correspond to the part of the root system growing within 7.5 mm to the O_2 optode from the binary image stack obtained by root segmentation from the NCL

dataset, and performed RSD calculation in this 3D-subvolume representing the 7.5 mm wide soil slice starting at the soil-optode interface. To obtain the surface area of the roots (in m^2), we first thinned the roots to their center line so that each root was only one voxel wide (skeletonization, plug-in “Skeletonize3D” in Fiji; <https://imagej.net/plugins/skeletonize3d>). We then applied the Euclidean distance transform (plug-in “Exact Euclidean Distance 3D” in Fiji (Schindelin et al., 2012), defined as the distance between the skeleton line and the border of the root, to obtain local root radius (R). From this 3D root radius map, S was calculated as $2\pi RL$ (where L is the pixelsize of $1.96 \times 10^{-4} \text{ m}$), assuming cylindrical root geometry (Kokko et al., 1993). Next, we projected the 3D root surface area map into one 2D image (“Z-Projection—maximum intensity”, ImageJ). Subsequently, RSD (m^2 root surface area m^{-3} soil volume) was derived by normalizing S by the corresponding soil volume (SV, 7.5 mm wide soil slice, Equation 1). Finally, water, gas, and solute exchange were projected and normalized for the 2D modeling approach (1 m thickness in y -direction of the simulation domain).

Root growth over the 52-h course of the experiment was neglected in this study for simplicity and because the set-up of the experiment was not equipped to measure root growth. Accordingly, RSD was assumed constant in all simulations and did not update over the course of the model runtime. The

resulting RSD map (Figure 4b), was converted to a MIN3P readable format and read into the model domain as follows:

$$\text{RSD}_i = \frac{S_i}{\text{SV}}, \quad (1)$$

where RSD_i = root surface density (m^2 root surface m^{-3} bulk soil) in control volume (i), S_i = root surface area (m^2), SV = soil volume (m^3) where the roots considered (frontal area of optode covered rhizotron area, 7.5 mm depth) are growing.

3.1.5 | Root water uptake

Spatially variable RWU Q_i was calculated based on the observed water loss from the rhizotron attributed to RWU ($\text{m}^3 \text{s}^{-1}$) and distributed across the domain as a function of RSD and saturation Equation 2, modified from Mayer et al. (2012).

$$Q_i = Q_{obs} \left(\frac{V_i \cdot \text{RSD}_i \cdot S_{a,i}}{\sum_{j=1, N_v} V_j \cdot \text{RSD}_j \cdot S_{a,j}} \right), \quad (2)$$

where Q_i is the volume of water removed over time from the domain by RWU ($\text{m}^3 \text{H}_2\text{O} \text{s}^{-1}$) in control volume (i); Q_{obs} ($\text{m}^3 \text{s}^{-1}$) is the soil water loss derived from the neutron images and is mathematically equivalent to the product of the total rate of root water uptake and the rhizotron surface area; V_i (m^3) is the control volume size; and $S_{a,i}$ is aqueous phase saturation ($\text{m}^3 \text{H}_2\text{O} \text{m}^{-3}$ void), calculated in-model, and N_v is the number of control volumes in the solution domain. We calibrated a water loss flux of $1.4 \times 10^{-8} \text{m}^3 \text{s}^{-1} \text{m}^{-2}$ to match observed water loss and moisture content distribution from the neutron image time series. This equation does not account for water stress, since moisture contents are relatively high throughout the experiment and preliminary simulations showed that the effect of water stress on the distribution of RWU is negligible.

3.1.6 | Root respiration

Two solute uptake mechanisms are considered in the presented simulations: “passive uptake”, considering removal of all dissolved species via RWU (i.e., Q_i ; Equation 2), and “direct uptake/release”, which includes processes like respiration, where solute is lost or gained by the roots independent of RWU. Most non-wetland plant species rely on direct uptake of molecular O_2 from the soil (Armstrong & Armstrong, 2014), as the quantity of dissolved O_2 that enters the root passively along with water uptake is insufficient to meet root respiratory demand (Ben-Noah & Friedman, 2018).

Direct uptake/release (Equation 3) was applied to simulate O_2 uptake and CO_2 release from the roots, assum-

ing a respiratory quotient of 1 (Hilman & Angert, 2016; Lambers et al., 2002), where 1 mol O_2 uptake leads to 1 mol CO_2 released per m^2 root. As autotrophic and heterotrophic respiration occur simultaneously in the rhizosphere and could not be separated clearly by our experimental approach, the O_2 uptake rate therefore included both root and rhizo-microbial O_2 uptake (and CO_2 release), respectively. We assumed all roots were capable of respiration to the same degree, and did not differentiate, for example, activity by root tip versus older root segments. For respiration (direct uptake/release), a zero-order sink term was calculated as follows:

$$Q_{k,i}^a = V_i \cdot k_k \cdot \text{RSD}_i, \quad (3)$$

where $Q_{k,i}^a$ (mol s^{-1}) considers loss (or gain) of a solute (k) via the root surface as a function of RSD_i (m^2 root surface m^{-3} bulk soil) in the control volume (i), with an assigned rate coefficient k_k (mol m^{-2} root surface s^{-1}) (in this case set as the uptake or release rate of O_2 , respectively CO_2 (k_{O_2} , respectively, k_{CO_2}) from the aqueous phase).

For this work, k_{O_2} was calibrated to a value of $2.5 \times 10^{-3} \text{mol m}^{-2}$ root surface s^{-1} for all simulations. For calibration, k_{O_2} was slowly increased until observed spatial and temporal concentration changes in O_2 in the domain were matched between the experiment (i.e., O_2 optode images) and the simulation. As a quantitative measure, we compared average O_2 concentration in the lower compartment between experiment and simulation and further adjusted k_{O_2} until NRMSE (normalized root mean square error) was below 0.5. NRMSE was calculated by normalizing RMSE to the difference between maximum and minimum O_2 concentrations from the experiment. To enable a numerical solution even at very low O_2 concentrations, uptake was limited to only occur above a threshold value of $1.0 \times 10^{-8} \text{mol L}^{-1} \text{H}_2\text{O}$. Once k_{O_2} was calibrated, CO_2 release was subsequently set as $k_{\text{CO}_2} = -k_{\text{O}_2}$.

The source–sink term for passive O_2 uptake was calculated as the product of local RWU and concentration of solute (k) per control volume (i) (Equation 4). For passive uptake:

$$Q_{k,i}^p = Q_i C_{k,i}, \quad (4)$$

where $Q_{k,i}^p$ (mol s^{-1}) is the source–sink for passive uptake per control volume (i), Q_i ($\text{m}^3 \text{H}_2\text{O} \text{s}^{-1}$) is RWU per control volume (i) previously calculated from Equation 2, and $C_{k,i}$ (mol m^{-3}) is the concentration of the solute (k) in control volume (i). Solute k includes all aqueous species present in the domain. As the geochemical system was simple and constrained to O_2 and CO_2 in the gaseous (g) and the aqueous (aq) phase, solute uptake was limited to these species and their secondary species and included $\text{O}_2(\text{aq})$, CO_3^{2-} , HCO_3^- , H_2CO_3 , OH^- , and H^+ . Further detail regarding gas phase partitioning

TABLE 2 Overview of the model scenarios. Simulations labeled “mapped” use a heterogeneous distribution of bulk soil parameters, as interpreted from moisture content data from the experiment (Equations 5–9; Figure 5).

Parameter	Model scenario		
	Model I	Model II	Model III
Barrier cracks	No	Yes	Yes
K_{sat}/ϕ	Homogeneous	Homogeneous	Mapped
n and α	Homogeneous	Homogeneous	Mapped

between the gas and aqueous phase and thermodynamic relationships for hydrolysis reactions considered may be found in the Supplementary Information Section S2.2.

3.1.7 | Boundary and initial conditions

The top boundary was set to a no-flow boundary condition as the plants were not watered after the start of the experiment and evaporation was assumed negligible. Gas exchange with the ambient air was enabled by a mixed upper boundary condition for reactive transport, with pO_2 and pCO_2 concentrations fixed at atmospheric levels in a boundary layer directly adjacent to the top of the upper compartment. The bottom boundary and both sides were also set as no-flow boundaries with no water, solute or gas exchange (Figure 1b), as the lateral sides were close to the impermeable side walls of the rhizotron and its base was sealed prior to initialization of the imaging experiment. The average initial hydraulic head in the lower compartment was estimated based on the soil moisture content measured 1 h after watering and the soil–water retention curve measured in the laboratory, and head set to 0.018 m. Initial O_2 concentration distribution was taken from the first optode image (1 h after rewetting) and read directly as an input file into the simulation. Due to differences in material characteristics, discrete values for moisture content and O_2 concentration in the barrier layer could not be determined as part of the image analysis. However, the raw image time series showed that initially, O_2 concentration in the barrier layer was low and increased toward the end of the experiment, whereas moisture content was highest in the beginning and declined until 52 h after rewetting. We inferred initial moisture content conditions based on material properties and defined initial head at the base, while barrier layer O_2 concentration was assumed negligible as an initial condition, and a sensitivity analysis was performed to rule out the possibility that these assumptions would strongly influence the results.

3.1.8 | Model scenarios based on experimental observations

We ran three simulations (Table 2), starting with a base model (Model I) and increasing bulk soil complexity con-

sidered in a stepwise fashion based on observations from the imaging experiment (Models II and III). The base model (Model I) assumed homogeneous bulk soil properties in the upper and lower compartment, together with a continuous and homogeneous barrier layer, with hydraulic parameters as described above (Table 1). However, detailed analysis of the neutron imaging data (both from 3D NCL and 2D radiography) revealed several crack structures, mainly located at the interface of the barrier layer (clayey material) and the glass of the rhizotron (see Figure 2). Based on the observation of these crack structures, we set up Model II, which included cracks with altered hydraulic properties next to the impermeable boundary on either side (see Supporting Information Section S3.1 for further parameterization of the cracks).

Model III was constructed based on another observation from the neutron images—after rewetting the soil, the neutron radiography showed that soil moisture was heterogeneously distributed (Figure 3). We considered that despite using material with a single grain size distribution, the inhomogeneous wetting and drying pattern could be caused by local differences in porosity due to the manual soil packing process, unintended mixing with finer-grained material from the barrier layer, and root growth. As such variability in total pore space would in turn result in spatially variable permeability as well as differences in pore water retention, Model III considered the impact of heterogeneous bulk soil characteristics on spatiotemporal evolution of moisture and O_2 concentration.

In addition to the crack structures from Model II, therefore, Model III considered heterogeneous permeability and porosity, mapped and correlated from observed soil moisture contents, as well as spatially variable soil hydraulic function parameters. Starting with a range of saturated hydraulic conductivities (K_{sat}) between $1.0 \times 10^{-6} \text{ m s}^{-1}$ and $1.0 \times 10^{-3} \text{ m s}^{-1}$, we assumed that zones of low moisture content by the end of the experiments (i.e., 52 h) were representative of zones where water may more easily flow toward the roots, and therefore has a higher permeability (and higher K_{sat}), whereas zones of higher moisture content near the end of the experiment indicated areas where water was released more slowly, and therefore represented material with lower permeability (lower K_{sat}). Under these assumptions and constrained by the range above, K_{sat} was calculated per control volume (i) from

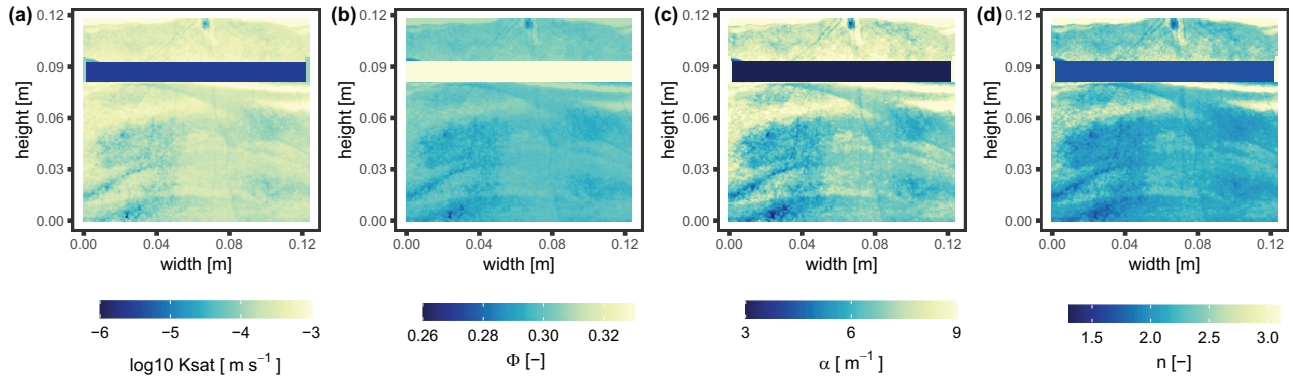


FIGURE 5 Heterogeneous K_{sat} (a), porosity ϕ (b), van Genuchten α (c), and van Genuchten n (d) mapped using moisture content data from the neutron radiograph captured 52 h after the initialization of the experiment. We emphasize that neutron radiography maps moisture content of all materials (soil and roots) along beam direction as summarized signal, so in regions with roots “soil moisture” contains root and soil water content. We did not distinguish regions with roots from regions without roots for calculation of hydraulic parameters for Model III, as the simulations were “upscaled” from pixel to control volume (3×3 pixels) and for simplicity. Values in the barrier layer were not mapped from neutron radiography but derived from Rosetta based on texture (Table 1).

experimental moisture content data as follows:

$$K_{\text{sat},i} = \left[K_{\text{sat,max}} - (K_{\text{sat,max}} - K_{\text{sat,min}}) \cdot \left(\frac{\theta_i - \theta_{\text{min}}}{\theta_{\text{max}} - \theta_{\text{min}}} \right) \right], \quad (5)$$

where $K_{\text{sat},i}$ is saturated hydraulic conductivity (m s^{-1}) in control volume (i), $K_{\text{sat,min}}$ and $K_{\text{sat,max}}$ define minimum and maximum K_{sat} for sandy soil, θ_{min} and θ_{max} are the minimum ($\theta_{\text{min}} < 0.01$) and maximum ($\theta_{\text{max}} = 0.28$) moisture contents measured in the experiment after 52 h, and θ_i is moisture content in the equivalent of control volume i from the experiment images (i.e., 3×3 pixel section), measured in the experiment after 52 h. Any K_{sat} values that fell above the defined range (e.g., those zones where cracks had clearly opened and held negligible moisture content) were assigned maximum K_{sat} values of $1.0 \times 10^{-3} \text{ m s}^{-1}$ (Figure 5a).

For consistency with heterogeneous permeability (K_{sat}), we associated higher porosity with higher K_{sat} (lower moisture content after 52 h), and estimated heterogeneous porosity distribution directly linked to heterogeneous permeability as follows:

$$\phi_i = \left[\phi_{\text{min}} + (\phi_{\text{max}} - \phi_{\text{min}}) \times \left(\frac{\log K_{\text{sat},i} - \log K_{\text{sat,min}}}{\log K_{\text{sat,max}} - \log K_{\text{sat,min}}} \right) \right], \quad (6)$$

where ϕ_i is porosity in control volume (i), and $K_{\text{sat},i}$ is calculated from Equation (5). Minimum and maximum porosities were bounded between 0.26 and 0.31 (Figure 5b). Porosity was correlated to permeability and not calculated directly

from moisture content because the distribution of aqueous saturation in the experiment was unknown.

For Model III, we also considered that a system with heterogeneous permeability and porosity would additionally be characterized by spatially variable soil hydraulic function parameters. We therefore spatially varied soil hydraulic function parameters α and n in the bulk soil (van Genuchten, 1980) (Figure 5c,d). Parameters α (units: Length^{-1} or kPa) and n (-) are empirical shape factors used to describe the soil–water characteristic curve (van Genuchten, 1980), where α functions as a scaling parameter related to the inverse of air entry pressure (for a drying soil) or water entry pressure (wetting soil), while n further relates to pore size distribution, with lower n values affiliated with greater variation in pore size (Benson et al., 2014). Effective saturation (S_a) is calculated as follows (van Genuchten, 1980):

$$S_a = S_r + \frac{1 - S_r}{[1 + (\alpha |\psi|)^n]^m}, \quad (7)$$

where S_r is the residual saturation, ψ is matric potential (m), and m is equal to $1 - n^{-1}$.

As parameters α and n are shape factors describing the soil–water characteristic curve, not representative of specific physical processes, previous works have suggested a variety of methods to calculate them based on texture, hydraulic conductivity, porosity, and other factors (e.g., Benson et al., 2014; Guarracino, 2007; Schaap et al., 2001; van Genuchten, 1980; Ye et al., 2021). We followed the method of Ye et al. (2021) to correlate α and n to K_{sat} locally as follows:

$$\alpha_i = 4.9 K_{\text{sat},i}^{0.23}, \quad (8)$$

$$n_i = 1.5 + 50 K_{\text{sat},i}^{0.5}, \quad (9)$$

where n_i (-) and α_i (kPa) are the van Genuchten shape parameters in control volume (i). Equations 8 and 9 are modified from Ye et al. (2021) (Figure 5c,d). In all simulations, hydraulic properties in the barrier layer were kept at the values given in Table 1 as no further information was available.

3.2 | Modeling results

We aimed to simulate O_2 concentration and soil moisture content as observed in the imaging experiment with a simple model first (Model I), where soil hydraulic and structural properties were homogenous throughout the domain. Model I captured the vertical soil moisture gradient from wetter conditions in the lower compartment to lower moisture in the upper compartment (Figure 6a). Average moisture content was within the range of that observed in the neutron measurements (considering an error margin of $\pm 10\%$ of the mean experimental data due to scattering artefacts in the neutron radiographs, shaded area in Figure 7a). However, the extensive spatial moisture content variation observed in the experiment could not be captured in this simulation (Figure 6a). Model I matched observed O_2 concentration well until 26 h after rewetting (Figures 6b and 7b), but failed to reproduce the O_2 ingress in the reentry zone and consequently differed from observations as of 26 h after rewetting.

The addition of cracks at the sides of the barrier layer in Model II showed only negligible effect on spatial distribution of soil moisture content compared to Model I (Figure 6a). In contrast, compared to Model I, Model II matched the basic O_2 pattern toward the end of the experiment (Figure 6b, second row) better. Beyond 26 h, ingress of O_2 through the cracks at the sides of the barrier layer facilitated re-oxygenation of the lower compartment, offsetting O_2 removal by the roots and associated O_2 depletion, in line with the experimental observations (Figure 6b, last row). However, the reentry zone was not as pronounced as seen in the optode images (Figure 7b), and O_2 depletion zones were not as sharply defined but rather diffuse, compared to the experimental observations (Figure 6b).

Observed moisture and O_2 concentration distributions were most closely reproduced by Model III, which, in addition to the cracks at the sides of the barrier layer, included mapped K_{sat} , porosity and heterogeneous distributions of the parameters α and n . Higher porosity zones, affiliated with higher α and n , retained water poorly, while other zones remained wetter, producing the soil moisture content distribution at the end of the simulation that was most similar to what was observed in the experiments (Figure 6a, Figure 7a). The resulting regions of higher and lower moisture content directly proximal to one another, allowed for zones of low O_2 concentration, where transport was considerably slowed in the

wetter soil, to coexist next to zones of very high O_2 concentration where, during re-oxygenation through the cracks, O_2 moved quickly through drier soil and contributed to the higher O_2 content. The combined mapping of porosity, permeability, and soil moisture retention parameters achieved the best match versus the O_2 image time-series, and also was closest to the absolute O_2 concentration in the lower compartment and the reentry zone (Figure 7b), suggesting that this level of model complexity is required to reproduce the spatially distributed evolution of moisture content and O_2 concentrations over time. Additional quantitative information on O_2 distribution for the various model realizations is provided in the Supporting Information Section S3.1 For the two other maize plants from the imaging experiment, results of Models I–III are given in the Supporting Information (Section S3.3) For these plants as well, Model III (mapped hydraulic parameters) showed the best agreement in the spatio-temporal distribution of water and O_2 content compared to the measured values (Figures S2 and S3).

CO_2 was considered in the model for completeness regarding respiration, although it was not measured in the experiment. The simulated pCO_2 pattern (Supporting Information Section S3.2) was more clearly impacted by the spatial location of roots versus the soil structure, compared to O_2 concentration (Figure 6b). However, model simulations showed higher CO_2 concentration toward the end of the simulation in Model III related to zones of increased water retention where CO_2 could accumulate, in contrast to the other simulations where CO_2 was more dispersed and lower concentrations were simulated (Supporting Information Figure S3.2). The presence of the barrier layer limited $CO_2(g)$ loss from the lower compartment, likewise contributing to high pCO_2 concentrations in the lower compartment compared to the upper compartment, where soil was able to degas. Further detail on results pertaining to CO_2 can be found in the Supporting Information Section S3.2.

4 | DISCUSSION

4.1 | Impact of bulk soil heterogeneity on modeled soil moisture and O_2 concentration patterns

The RT models presented in this study were constructed based on spatial and structural information on the RSA of a maize plant derived from 3D neutron imaging, and were calibrated to match moisture content and O_2 concentration patterns measured via neutron radiography and optode imaging. In the experiment, a barrier layer of fine-grained material separated the soil domain into two distinct compartments, and restricted O_2 transport toward the roots in the lower compartment. Due to the drying–rewetting cycle during the experiment, several crack structures formed in this layer. Inclusion of small

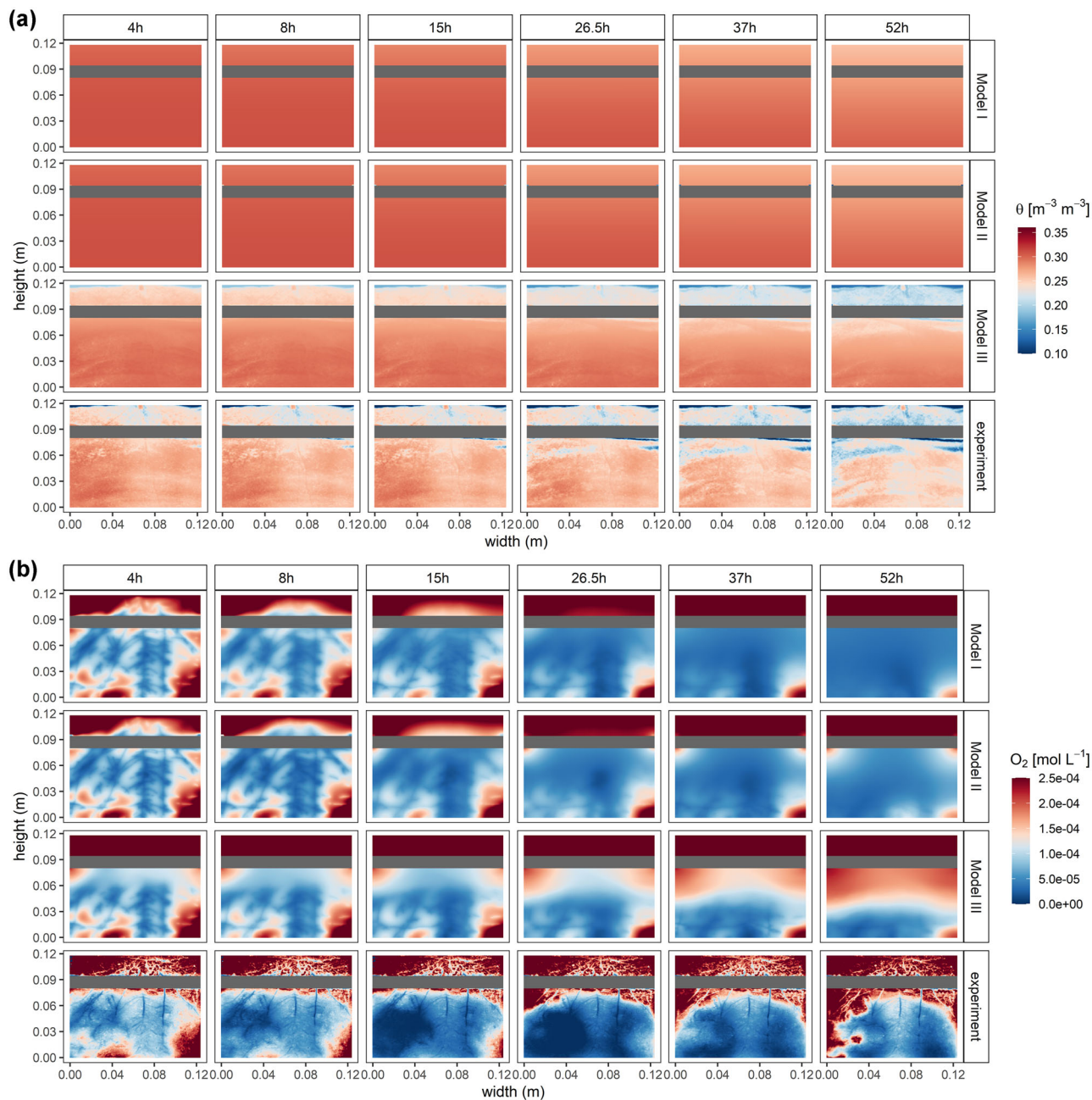


FIGURE 6 Spatial distribution of soil moisture (a) and oxygen (O_2) concentration (b) at different times after rewetting the soil for Models I–III and corresponding experimental results. Both optode and neutron images were calibrated only for the sandy soil material, not for the barrier layer (indicated as gray area in the plots), so a quantitative comparison of experiment versus models was not possible for the barrier layer. In Models I and II, the soil domain was homogenous in terms of hydraulic parameters and porosity; in Model II zones of high permeability were introduced at each side of the barrier layer based on observed crack formation from image analysis. Agreement between modeled and observed experimental distribution of θ (volumetric moisture content) and O_2 concentration was highest in Model III where soil porosity and hydraulic parameters (K_{sat} and van Genuchten α and n) were mapped based on the neutron image time series.

zones of high porosity and increased hydraulic conductivity (K_{sat}) in the model barrier layer, representative of the cracks observed, did facilitate O_2 ingress into the lower compartment. Simulations taking into consideration the presence of cracks (Model II and III) matched the O_2 pattern in the experiment more closely compared to Model I (no cracks). This

was specifically evident in the distinct O_2 “reentry zones” observed in the optode images (>15 h after rewetting). This result highlights that soil macropore structures impact soil gas transport, as supported by insights from X-ray imaging studies combined with measurement of gas transport and air permeability (Katuwal et al., 2015; Naveed et al., 2013), as well

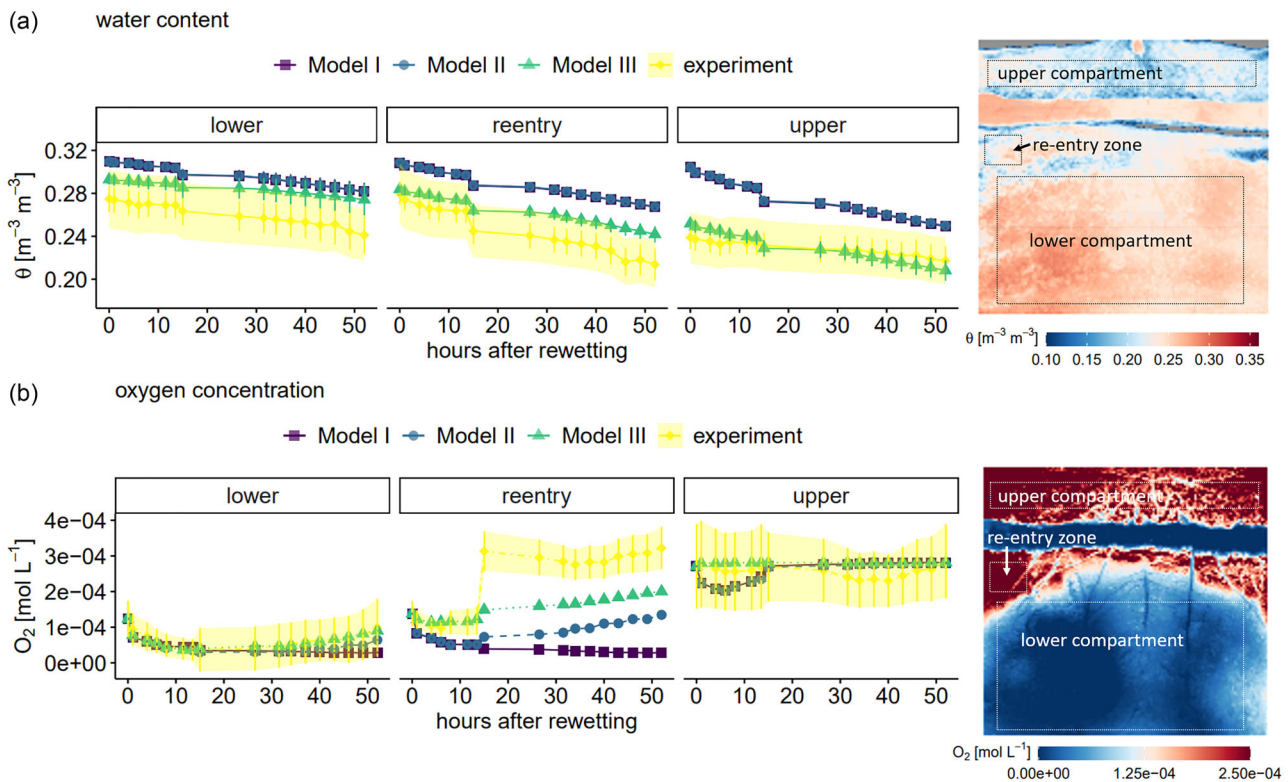


FIGURE 7 Comparison of measured and simulated soil moisture content and oxygen (O_2) concentration in the lower compartment, the O_2 reentry zone, and the upper compartment. Measured and simulated water content (a) and O_2 concentration (b) from Model I, II and III (averaged across the regions outlined in gray on the image on the right) are compared to the experimental values. The error bars indicate ± 1 standard deviation from the mean. The shaded yellow area in (a) indicates $\pm 10\%$ of the mean to represent signal variations due to secondary neutron scattering and in (b) indicates ± 1 standard deviation from O_2 concentration.

as field measurements of soil aeration related to root-induced macropore networks (Uteau et al., 2013).

Consideration of heterogeneous permeability and porosity in the upper and lower compartments (Model III) enabled modeling of spatially distributed soil moisture patterns, in-line with the experimental observations. At different scales, several studies indicate that local variations of soil physical properties, specifically bulk density (and thereby total porosity) (Hamamoto et al., 2009; Masís-Meléndez et al., 2015), impact water retention, gas diffusion, and O_2 concentration present in the soil (Ben-Noah & Friedman, 2018). Soil layering during manual filling of the rhizotrons in the present experiment, as well as root growth, which can induce local soil compaction, especially in homogenized soils (Phalempin et al., 2021), have likely contributed to local variations of porosity (bulk density).

Additional mapping of VG α and n in Model III, based on the heterogeneous wetting patterns evident in the neutron radiographs, improved spatial simulation of moisture content because it allowed the simulations to account for small-scale variability in terms of moisture retention, producing zones of higher permeability and faster drainage, as well as zones of prolonged moisture retention, reflecting the heterogeneous

moisture content distribution in the experiment. As modeled, such heterogeneity in moisture content was key to reproducing the O_2 concentration distribution toward the end of the experiment, with O_2 diffusion only slowed in distinct wet zones, reproducing persistent local O_2 depletion, while the drier soil, where O_2 could diffuse quickly, reapproached atmospheric concentration levels.

Such results speak to the necessity and the benefit of considering system-specific heterogeneities that may be neglected in bulk-scale conceptual models. Yet, calibrating soil structural and hydraulic characteristics based on experimental data is challenging and, despite detailed spatial and temporal data, is still affected by uncertainty. To better account for variability in soil structure, we suggest that the presented combination of neutron and optode imaging would benefit from additional application of X-ray tomography, a method that is ideal for studying soil structure at high resolution (Lucas et al., 2019) and that has also been applied to derive soil water retention and K_{sat} in rooted soils in 3D (Tracy et al., 2015). Further, a full calibration of the water retention curves of drying and rewetting soil via neutron radiography, as presented by Cheng et al. (2012), could be a useful extension for follow-up studies.

4.2 | Representation of root system and rhizosphere complexity in the models

Roots were modeled via the spatial distribution of RSD as derived from structural 3D imaging (NCL), and spatial O₂ uptake patterns evolved where higher root density consumed more O₂. For modeling root O₂ uptake, both a zero-order (independent of actual O₂ concentration) or a first-order sink term (i.e. dependent on changing O₂ concentration) can be considered (Ben-Noah & Friedman, 2018). In this study, a zero-order O₂ consumption rate that was restricted by a lower threshold of minimum O₂ concentration, was found suitable to simulate observed O₂ depletion zones similar to the experiment. However, it is known that root age, physiological function, N content and distance from the root tip impact root respiration rates (Freschet et al., 2021). A model of a sub-domain of the root system might therefore need further refinement of the representation of respiration rate variations within the root system and over time. However, we find from this work that for plant-scale models focusing on water and gas transport dynamics, a uniform O₂ sink term may suffice. The same applies for the simulation of root water uptake: to represent the general pattern of moisture distribution and the mass balance of water uptake in the rhizotron system, a sink term for water uptake scaled to the RSD per control volume was adequate. Depending on the research question, further refinement of RWU simulation might be required, for example to understand variation in RWU between root types.

Our modeling approach did not explicitly consider structural and hydraulic characteristics of the rhizosphere, although the rhizosphere is known to feature unique physical, hydraulic and chemical properties, differing from those of the bulk soil (Hinsinger et al., 2005). Hydraulic properties and diffusion of gases in the rhizosphere are impacted by hydrogel substances excreted by roots and microbes, particularly mucilage (Benard et al., 2019), a highly viscous substance made up of polysaccharides. While the mucilage layer around roots facilitates water uptake (Ahmed et al., 2014) and nutrient diffusion (Zarebanadkouki et al., 2019) in drying soils, gas transport to the roots' surface is impeded as the O₂ diffusion coefficient within this layer is estimated to be as low as $2 \times 10^{-10} \text{ m}^2 \text{ s}^{-1}$ and O₂ solubility is limited (Ben-Noah & Friedman, 2018). Drying mucilage may also disconnect gas diffusion paths even at low soil water content (Haupenthal et al., 2021). At the micro-scale, several models of O₂ root uptake and transport consider a 'boundary layer' of saturated soil surrounding the roots to account for limited diffusion in the rhizosphere soil (Bartholomeus et al., 2008; Cook & Knight, 2003). In our plant-scale model, we did not explicitly consider the rhizosphere or mucilage layer's distinct hydraulic and diffusive properties. This approach was sufficient for characterizing the 2D spatial distribution of O₂ in the root zone of the maize plant in our work. However, we suggest

that simulations of O₂ uptake at the root scale, particularly those featuring drier systems, would benefit from a simplified implementation of a distinct rhizosphere zone where diffusion parameters could be adapted versus the bulk soil.

4.3 | Representing a 3D root–soil system in a 2D model

While structural information about the root system of the modeled maize plant was available in 3D, O₂ and moisture content were mapped in 2D using imaging techniques that, due to their mode of operation, aggregate information from different sub-volumes of the experimental system. The optode images represent a depth-integrated response of O₂ dynamics across a variable portion of the root–soil system under consideration, which adds uncertainty regarding which portion of the root system triggers observed patterns at a specific point in time (Roose et al., 2016). As in a previous study using a comparable experimental set-up, where O₂ uptake of roots growing within a distance of 7.5 mm to the optode was measured a few hours after irrigation of dry soil (Rudolph-Mohr et al., 2021), we assumed that the roots located within this soil volume were sufficiently representative of the root system in the presented model, as we aimed to compare optode images and 2D model output. Though we find this a necessary simplification, the influence of the entire root system in terms of the observed O₂ depletion pattern merits further investigation, possibly in a 3D modeling approach. Likewise, as neutron radiography provides a depth-integrated neutron transmission signal across the sample's thickness and consequently maps the sum of the water content of all structures superimposed in beam direction, the exact soil moisture content in different soil sub-volumes relative to the optode also cannot be quantified with this approach. For this work, neutron radiography revealed the overall spatial distribution and heterogeneity of soil water content that correlated well with local O₂ concentration patterns in both experiment and model. Future studies could target extending our model approach to 3D in order to better spatially correlate moisture content and O₂ depletion to individual roots.

4.4 | Potential and challenges of combining non-invasive imaging and reactive transport modeling

Due to the complex and cross-scale nature and spatiotemporal variability of transport processes and reactions in the root zone, the combination of three different non-invasive imaging techniques with RT modeling, as presented here, enables detailed spatiotemporal analysis of root zone O₂ and moisture dynamics. While RSA derived from different imaging modalities is increasingly used as input for modeling of root

water and nutrient uptake and exudation (Daly et al., 2016; McKay Fletcher et al., 2020), only a few modeling studies make use of image-based observations of spatially resolved solute, gas, or pH distribution in the root zone (Custos et al., 2020) and no comparable studies on O₂ uptake and transport dynamics in the root zone exist. This work emphasizes the potential that such a combined approach may bring to furthering understanding of root–soil dynamics in-situ on the plant scale, without necessitating invasive and destructive measurement techniques. This work suggests that O₂ distribution follows more closely to soil structure than root distribution, and we submit that the influence of bulk soil heterogeneity on water and gas transport dynamics in the root zone should be considered in models at the plant scale, and that work should be done to determine sensitive parameters in the bulk soil when modeling such systems. Identifying sensitive parameters presents its own set of difficulties, and we find in this work the combination of non-invasive imaging along with modeling, to function together as a powerful tool to qualitatively and quantitatively identify such complexities of note in a soil–root system.

As highlighted by Roose et al. (2016), the combination of imaging and modeling allows model generation based on real data, with the caveat that such models might always be specifically adapted to a certain experimental system (Dale et al., 2021). For this work specifically, we found that inclusion of bulk soil heterogeneity was necessary to characterize the experimental system using an RT model, and that doing so increased our understanding of the dynamics of water redistribution and O₂ transport as a function of root uptake. However, we suggest that the exact complexities and heterogeneities (e.g. cracks, variable porosity and permeability, and VG shape factors) necessary to best characterize this particular experimental system, may not be the same as those complexities needed to best characterize other systems. Indeed, future models based off the methodology of this work, would need to be carefully revised with respect to the discussed assumptions and simplifications, when applied to other soil–plant systems. Further, the models' complexity needs to be tailored to answer the research question to be explored.

5 | CONCLUSIONS

This study focused on the interrelation between O₂ transport, soil moisture, and respiration in the root-zone of a maize plant grown in a rhizotron system. Our approach bridges the gap between experimental measurement of small-scale gradients in the rhizosphere via noninvasive imaging, and modeling of overarching transport and uptake processes that explain observed patterns of O₂ and soil moisture. Via iterative construction of different model scenarios, we show that a model can better characterize the studied plant–soil system when we

consider conditions unique to the system in question; in this case, crack structures in the soil and spatial heterogeneity in soil structure and water retention properties. Additionally, we find that though the focus of the imaging and the modeling was on depicting root architecture and concentration patterns in great detail, in terms of future soil–root modeling prospects, the importance of the soil physical parameters should be given an equivalent amount of attention and consideration. As the scientific community moves forward in constructing additional soil–plant models using field and laboratory data, this work can be helpful for making future choices regarding the degree of model complexity that can capably characterize the geochemistry of a soil–root system, given the limits of existing data, as well as inform future decisions regarding where efforts in data collection could best be spent.

AUTHOR CONTRIBUTIONS

Sarah Bereswill: Conceptualization; formal analysis; investigation; visualization; writing—original draft. **Hannah Gatz-Miller:** Conceptualization; formal analysis; methodology; writing—original draft. **Danyang Su:** Software; writing—review and editing. **Christian Tötzke:** Investigation; writing—review and editing. **Nikolay Kardjilov:** Investigation; resources. **Sascha E. Oswald:** Supervision; writing—review and editing. **K. Ulrich Mayer:** Supervision; writing—review and editing.

ACKNOWLEDGMENTS

The authors would like to thank the following colleagues from Institute of Environmental Science and Geography, University of Potsdam: Dr. Nicole Rudolph-Mohr for preparation of beamtime proposal and guidance on plant growth and imaging experiment, Peter Biro and Boyana Kozuharova for help on conducting the plant imaging experiment, and Lena Scheiffle for laboratory analysis of soil texture and water retention curve. The authors would like to thank Dr. André Hilger (Institute of Applied Materials, Helmholtz Centre Berlin for Energy and Materials) for help with neutron computed laminography reconstruction. The authors gratefully acknowledge funding of the research presented here by the German Research Foundation (DFG) under Grant Numbers OS 351/8-1 and TO 949/2-1, project no. 396368046. Funded by the Deutsche Forschungsgemeinschaft (DFG, German Research Foundation) – Projektnummer 491466077.

CONFLICT OF INTEREST STATEMENT

The authors declare no conflicts of interest.

ORCID

Sarah Bereswill  <https://orcid.org/0000-0001-6165-9448>
Hannah Gatz-Miller  <https://orcid.org/0000-0002-1339-6249>

Danyang Su  <https://orcid.org/0000-0003-0622-9319>
 Christian Tötze  <https://orcid.org/0000-0001-8246-4375>
 Nikolay Kardjilov  <https://orcid.org/0000-0002-0980-1440>
 Sascha E. Oswald  <https://orcid.org/0000-0003-1667-0060>
 Klaus Ulrich Mayer  <https://orcid.org/0000-0002-4168-781X>

REFERENCES

- Ahmed, M. A., Kroener, E., Holz, M., Zarebanadkouki, M., & Carminati, A. (2014). Mucilage exudation facilitates root water uptake in dry soils. *Functional Plant Biology*, *41*(11), 1129–1137. <https://doi.org/10.1071/FP13330>
- Armstrong, W., & Armstrong, J. (2014). Plant internal oxygen transport (diffusion and convection) and measuring and modelling oxygen gradients. In J. T. van Dongen, & F. Licausi (Eds.), *Low-oxygen stress in plants: Oxygen sensing and adaptive responses to hypoxia* (pp. 267–297). https://doi.org/10.1007/978-3-7091-1254-0_14
- Bartholomeus, R. P., Witte, J.-P. M., van Bodegom, P. M., van Dam, J. C., & Aerts, R. (2008). Critical soil conditions for oxygen stress to plant roots: Substituting the Feddes-function by a process-based model. *Journal of Hydrology*, *360*(1–4), 147–165. <https://doi.org/10.1016/j.jhydrol.2008.07.029>
- Benard, P., Zarebanadkouki, M., Brax, M., Kaltenbach, R., Jerjen, I., Marone, F., Couradeau, E., Felde, V. J. M. N. L., Kaestner, A., & Carminati, A. (2019). Microhydrological niches in soils: How mucilage and EPS alter the biophysical properties of the rhizosphere and other biological hotspots. *Vadose Zone Journal*, *18*(1), 1–10. <https://doi.org/10.2136/vzj2018.12.0211>
- Ben-Noah, I., & Friedman, S. P. (2018). Review and evaluation of root respiration and of natural and agricultural processes of soil aeration. *Vadose Zone Journal*, *17*(1), 1–47. <https://doi.org/10.2136/vzj2017.06.0119>
- Benson, C. H., Chiang, I., Chalermyanont, T., & Sawangsuriya, A. (2014). Estimating van Genuchten parameters α and n for clean sands from particle size distribution data. *From Soil Behavior Fundamentals to Innovations in Geotechnical Engineering* (pp. 410–427). ASCE. <https://doi.org/10.1061/9780784413265.033>
- Blossfeld, S., Schreiber, C. M., Liebsch, G., Kuhn, A. J., & Hinsinger, P. (2013). Quantitative imaging of rhizosphere pH and CO₂ dynamics with planar optodes. *Annals of Botany*, *112*(2), 267–276. <https://doi.org/10.1093/aob/mct047>
- Braghiere, R. K., Gérard, F., Evers, J. B., Pradal, C., & Pagès, L. (2020). Simulating the effects of water limitation on plant biomass using a 3D functional–structural plant model of shoot and root driven by soil hydraulics. *Annals of Botany*, *126*(4), 713–728. <https://doi.org/10.1093/aob/mcaa059>
- Cheng, C. L., Kang, M., Perfect, E., Voisin, S., Horita, J., Bilheux, H. Z., Warren, J. M., Jacobson, D. L., & Hussey, D. S. (2012). Average soil water retention curves measured by neutron radiography. *Soil Science Society of America Journal*, *76*(4), 1184–1191. <https://doi.org/10.2136/sssaj2011.0313>
- Cook, F. J., & Knight, J. H. (2003). Oxygen transport to plant roots. *Soil Science Society of America Journal*, *67*(1), 20–31. <https://doi.org/10.2136/sssaj2003.2000>
- Cook, F. J., Knight, J. H., & Kelliher, F. M. (2013). Modelling oxygen transport in soil with plant root and microbial oxygen consumption: Depth of oxygen penetration. *Soil Research*, *51*(6), 539. <https://doi.org/10.1071/SR13223>
- Custos, J.-M., Moyne, C., & Sterckeman, T. (2020). How root nutrient uptake affects rhizosphere pH: A modelling study. *Geoderma*, *369*(2020), 114314. <https://doi.org/10.1016/j.geoderma.2020.114314>
- Dale, R., Oswald, S., Jalihal, A., LaPorte, M.-F., Fletcher, D. M., Hubbard, A., Shiu, S. H., Nelson, A. D. L., & Bucksch, A. (2021). Overcoming the challenges to enhancing experimental plant biology with computational modeling. *Frontiers in Plant Science*, *12*, 687652. <https://doi.org/10.3389/fpls.2021.687652>
- Daly, K. R., Keyes, S. D., Masum, S., & Roose, T. (2016). Image-based modelling of nutrient movement in and around the rhizosphere. *Journal of Experimental Botany*, *67*(4), 1059–1070. <https://doi.org/10.1093/jxb/erv544>
- Dettmann, U. (2022). *SoilHyP: Soil hydraulic properties*. R package version 0.1.6. <https://cran.r-project.org/package=SoilHyP>
- Drew, M., & Armstrong, W. (2002). Root growth and metabolism under oxygen deficiency. *Plant roots: The hidden half* (3rd ed., pp. 729–761). CRC Press. <https://doi.org/10.1201/9780203909423>
- Espeleta, J. F., Cardon, Z. G., Mayer, K. U., & Neumann, R. B. (2017). Diel plant water use and competitive soil cation exchange interact to enhance NH₄⁺ and K⁺ availability in the rhizosphere. *Plant and Soil*, *414*(1–2), 33–51. <https://doi.org/10.1007/s11104-016-3089-5>
- Freschet, G. T., Pagès, L., Iversen, C. M., Comas, L. H., Rewald, B., Roumet, C., Klimešová, J., Zadworny, M., Poorter, H., Postma, J. A., Adams, T. S., Bagniewska-Zadworna, A., Bengough, A. G., Blancaflor, E. B., Brunner, I., Cornelissen, J. H. C., Garnier, E., Gessler, A., Hobbie, S. E., ... McCormack, M. L. (2021). A starting guide to root ecology: Strengthening ecological concepts and standardising root classification, sampling, processing and trait measurements. *New Phytologist*, *232*(3), 973–1122. <https://doi.org/10.1111/nph.17572>
- Gatz-Miller, H. S., Gérard, F., Verrecchia, E. P., Su, D., & Mayer, K. U. (2022). Reactive transport modelling the oxalate-carbonate pathway of the Iroko tree; Investigation of calcium and carbon sinks and sources. *Geoderma*, *410*, 115665. <https://doi.org/10.1016/j.geoderma.2021.115665>
- Gérard, F., Mayer, K. U., Hodson, M. J., & Ranger, J. (2008). Modelling the biogeochemical cycle of silicon in soils: Application to a temperate forest ecosystem. *Geochimica et Cosmochimica Acta*, *72*(3), 741–758. <https://doi.org/10.1016/j.gca.2007.11.010>
- Gérard, F., Blitz-Frayret, C., Hinsinger, P., & Pagès, L. (2017). Modelling the interactions between root system architecture, root functions and reactive transport processes in soil. *Plant and Soil*, *413*(1–2), 161–180. <https://doi.org/10.1007/s11104-016-3092-x>
- Guarracino, L. (2007). Estimation of saturated hydraulic conductivity Ks from the van Genuchten shape parameter α . *Water Resources Research*, *43*(11), 15–18. <https://doi.org/10.1029/2006WR005766>
- Haber-Pohlmeier, S., Tötze, C., Lehmann, E., Kardjilov, N., Pohlmeier, A., & Oswald, S. E. (2019). Combination of magnetic resonance imaging and neutron computed tomography for three-dimensional rhizosphere imaging. *Vadose Zone Journal*, *18*(1), 1–11. <https://doi.org/10.2136/vzj2018.09.0166>
- Hamamoto, S., Moldrup, P., Kawamoto, K., & Komatsu, T. (2009). Effect of particle size and soil compaction on gas transport parameters in variably saturated, sandy soils. *Vadose Zone Journal*, *8*(4), 986–995. <https://doi.org/10.2136/vzj2008.0157>
- Haupenthal, A., Brax, M., Bentz, J., Jungkunst, H. F., Schützenmeister, K., & Kroener, E. (2021). Plants control soil gas exchanges possibly

- via mucilage. *Journal of Plant Nutrition and Soil Science*, 184(3), 320–328. <https://doi.org/10.1002/jpln.202000496>
- Helfen, L., Xu, F., Schillinger, B., Calzada, E., Zanette, I., Weitkamp, T., & Baumbach, T. (2011). Neutron laminography—A novel approach to three-dimensional imaging of flat objects with neutrons. *Nuclear Instruments and Methods in Physics Research Section A: Accelerators, Spectrometers, Detectors and Associated Equipment*, 651(1), 135–139. <https://doi.org/10.1016/j.nima.2011.01.114>
- Hilman, B., & Angert, A. (2016). Measuring the ratio of CO₂ efflux to O₂ influx in tree stem respiration. *Tree Physiology*, 36(11), 1422–1431. <https://doi.org/10.1093/treephys/tpw057>
- Hinsinger, P., Gobran, G. R., Gregory, P. J., & Wenzel, W. W. (2005). Rhizosphere geometry and heterogeneity arising from root-mediated physical and chemical processes. *New Phytologist*, 168(2), 293–303. <https://doi.org/10.1111/j.1469-8137.2005.01512.x>
- Holz, M., Zarebanadkouki, M., Carminati, A., & Kuz'yakov, Y. (2019). Visualization and quantification of root exudation using 14C imaging: Challenges and uncertainties. *Plant and Soil*, 437(1–2), 473–485. <https://doi.org/10.1007/s11104-019-03956-8>
- Iden, S. C., & Durner, W. (2008). Free-Form estimation of soil hydraulic properties using Wind's method. *European Journal of Soil Science*, 59(6), 1228–1240. <https://doi.org/10.1111/j.1365-2389.2008.01068.x>
- Jia, M., Jacques, D., Gérard, F., Su, D., Mayer, K. U., & Šimůnek, J. (2021). A benchmark for soil organic matter degradation under variably saturated flow conditions. *Computational Geosciences*, 25(4), 1359–1377. <https://doi.org/10.1007/s10596-019-09862-3>
- Kardjilov, N., Hilger, A., Manke, I., Woracek, R., & Banhart, J. (2016). CONRAD-2: The new neutron imaging instrument at the Helmholtz-Zentrum Berlin. *Journal of Applied Crystallography*, 49(1), 195–202. <https://doi.org/10.1107/S1600576715023353>
- Katuwal, S., Norgaard, T., Moldrup, P., Lamandé, M., Wildenschild, D., & de Jonge, L. W. (2015). Linking air and water transport in intact soils to macropore characteristics inferred from X-ray Computed Tomography. *Geoderma*, 237–238, 9–20. <https://doi.org/10.1016/j.geoderma.2014.08.006>
- Kokko, E. G., Volkmar, K. M., Gowen, B. E., & Entz, T. (1993). Determination of total root surface area in soil core samples by image analysis. *Soil and Tillage Research*, 26(1), 33–43. [https://doi.org/10.1016/0167-1987\(93\)90084-3](https://doi.org/10.1016/0167-1987(93)90084-3)
- Lambers, H., Atkin, O., & Millenaar, F. (2002). Respiratory patterns in roots in relation to their functioning. In Y. Waisel, A. Eshel, T. Beeckman, & U. Kafkafai (Eds.), *Plant roots: The hidden half* (3rd ed., pp. 521–552). CRC Press. <https://doi.org/10.1201/9780203909423>
- Lambers, H., Clements, J. C., & Nelson, M. N. (2013). How a phosphorus-acquisition strategy based on carboxylate exudation powers the success and agronomic potential of lupines (*Lupinus*, Fabaceae). *American Journal of Botany*, 100(2), 263–288. <https://doi.org/10.3732/ajb.1200474>
- Li, L., Maher, K., Navarre-Sitchler, A., Druhan, J., Meile, C., Lawrence, C., Moore, J., Perdrial, J., Sullivan, P., Thompson, A., Jin, L., Bolton, E. W., Brantley, S. L., Dietrich, W. E., Mayer, K. U., Steefel, C. I., Valocchi, A., Zachara, J., Kocar, B., ... Beisman, J. (2017). Expanding the role of reactive transport models in critical zone processes. *Earth-Science Reviews*, 165, 280–301. <https://doi.org/10.1016/j.earscirev.2016.09.001>
- Lucas, M., Schlüter, S., Vogel, H.-J., & Vetterlein, D. (2019). Roots compact the surrounding soil depending on the structures they encounter. *Scientific Reports*, 9(1), 16236. <https://doi.org/10.1038/s41598-019-52665-w>
- Masís-Meléndez, F., de Jonge, L. W., Chamindu Deepagoda, T. K. K., Tuller, M., & Moldrup, P. (2015). Effects of soil bulk density on gas transport parameters and pore-network properties across a sandy field site. *Vadose Zone Journal*, 14(7), 1–12. <https://doi.org/10.2136/vzj2014.09.0128>
- Mayer, K. U., Amos, R. T., Molins, S., & Gérard, F. (2012). Reactive transport modeling in variably saturated media with MIN3P: Basic model formulation and model enhancements. In K. U. Mayer, R. T. Amos, S. Molins, & F. Gerard (Eds.), *Groundwater reactive transport models* (pp. 186–211). Bentham Science Publisher. <https://doi.org/10.2174/978160805306311201010186>
- Mayer, K. U., Frind, E. O., & Blowes, D. W. (2002). Multicomponent reactive transport modeling in variably saturated porous media using a generalized formulation for kinetically controlled reactions. *Water Resources Research*, 38(9), 13–1–13–21. <https://doi.org/10.1029/2001WR000862>
- Mayer, K. U., & MacQuarrie, K. T. B. (2010). Solution of the MoMaS reactive transport benchmark with MIN3P-model formulation and simulation results. *Computational Geosciences*, 14(3), 405–419. <https://doi.org/10.1007/s10596-009-9158-6>
- Mayer, K. U., Xie, M., Su, D., Vt, C., & Macquarrie, K. (2015). *A three-dimensional numerical model for multicomponent reactive transport in variably saturated porous media. User guide*. <https://www.min3p.com/contact-us>
- McKay Fletcher, D. M., Ruiz, S., Dias, T., Petroselli, C., & Roose, T. (2020). Linking root structure to functionality: The impact of root system architecture on citrate-enhanced phosphate uptake. *New Phytologist*, 227(2), 376–391. <https://doi.org/10.1111/nph.16554>
- Millington, R. J. (1959). Gas diffusion in porous media author. 130(3367), 100–102. <http://www.jstor.org/stable/1757604>
- Moradi, A. B., Oswald, S. E., Nordmeyer-Massner, J. A., Pruessmann, K. P., Robinson, B. H., & Schulin, R. (2010). Analysis of nickel concentration profiles around the roots of the hyperaccumulator plant *Berkheya coddii* using MRI and numerical simulations. *Plant and Soil*, 328(1–2), 291–302. <https://doi.org/10.1007/s11104-009-0109-8>
- Naveed, M., Moldrup, P., Arthur, E., Wildenschild, D., Eden, M., Lamandé, M., Vogel, H., & de Jonge, L. W. (2013). Revealing soil structure and functional macroporosity along a clay gradient using X-ray Computed Tomography. *Soil Science Society of America Journal*, 77(2), 403–411. <https://doi.org/10.2136/sssaj2012.0134>
- Neira, J., Ortiz, M., Morales, L., & Acevedo, E. (2015). Oxygen diffusion in soils: Understanding the factors and processes needed for modeling. *Chilean Journal of Agricultural Research*, 75, 35–44. <https://doi.org/10.4067/S0718-58392015000300005>
- Nowack, B., Mayer, K. U., Oswald, S. E., van Beinum, W., Appelo, C. A. J., Jacques, D., Seuntjens, P., Gérard, F., Jaillard, B., Schnepf, A., & Roose, T. (2006). Verification and intercomparison of reactive transport codes to describe root-uptake. *Plant and Soil*, 285(1–2), 305–321. <https://doi.org/10.1007/s11104-006-9017-3>
- Oswald, S. E., Menon, M., Carminati, A., Vontobel, P., Lehmann, E., & Schulin, R. (2008). Quantitative Imaging of Infiltration, Root Growth, and Root Water Uptake via Neutron Radiography. *Vadose Zone Journal*, 7(3), 1035–1047. <https://doi.org/10.2136/vzj2007.0156>
- Pagès, L., Bécel, C., Boukcim, H., Moreau, D., Nguyen, C., & Voisin, A.-S. (2014). Calibration and evaluation of ArchiSimple, a simple model of root system architecture. *Ecological Modelling*, 290, 76–84. <https://doi.org/10.1016/j.ecolmodel.2013.11.014>

- Peters, A., & Durner, W. (2008). Simplified evaporation method for determining soil hydraulic properties. *Journal of Hydrology*, 356(1–2), 147–162. <https://doi.org/10.1016/j.jhydrol.2008.04.016>
- Phalempin, M., Lippold, E., Vetterlein, D., & Schlüter, S. (2021). Soil texture and structure heterogeneity predominantly governs bulk density gradients around roots. *Vadose Zone Journal*, 20(5), 1–17. <https://doi.org/10.1002/vzj2.20147>
- Roose, T., Keyes, S. D., Daly, K. R., Carminati, A., Otten, W., Vetterlein, D., & Peth, S. (2016). Challenges in imaging and predictive modeling of rhizosphere processes. *Plant and Soil*, 407(1–2), 9–38. <https://doi.org/10.1007/s11104-016-2872-7>
- Rudolph-Mohr, N., Bereswill, S., Tötze, C., Kardjilov, N., & Oswald, S. E. (2021). Neutron computed laminography yields 3D root system architecture and complements investigations of spatiotemporal rhizosphere patterns. *Plant and Soil*, 469(1–2), 489–501. <https://doi.org/10.1007/s11104-021-05120-7>
- Rudolph-Mohr, N., Tötze, C., Kardjilov, N., & Oswald, S. E. (2017). Mapping water, oxygen, and pH dynamics in the rhizosphere of young maize roots. *Journal of Plant Nutrition and Soil Science*, 180(3), 336–346. <https://doi.org/10.1002/jpln.201600120>
- Rudolph-Mohr, N., Vontobel, P., & Oswald, S. E. (2014). A multi-imaging approach to study the root-soil interface. *Annals of Botany*, 114(8), 1779–1787. <https://doi.org/10.1093/aob/mcu200>
- Schaap, M. G., Leij, F. J., & van Genuchten, M. T. (2001). rosetta: A computer program for estimating soil hydraulic parameters with hierarchical pedotransfer functions. *Journal of Hydrology*, 251(3–4), 163–176. [https://doi.org/10.1016/S0022-1694\(01\)00466-8](https://doi.org/10.1016/S0022-1694(01)00466-8)
- Schindelin, J., Arganda-Carreras, I., Frise, E., Kaynig, V., Longair, M., Pietzsch, T., Preibisch, S., Rueden, C., Saalfeld, S., Schmid, B., Tinevez, J. Y., White, D. J., Hartenstein, V., Eliceiri, K., Tomancak, P., & Cardona, A. (2012). Fiji: An open-source platform for biological-image analysis. *Nature Methods*, 9(7), 676–682. <https://doi.org/10.1038/nmeth.2019>
- Schmitz, D., Anlauf, R., & Rehrmann, P. (2013). Effect of air content on the oxygen diffusion coefficient of growing media. *American Journal of Plant Sciences*, 04(05), 955–963. <https://doi.org/10.4236/ajps.2013.45118>
- Schneider, C. A., Rasband, W. S., & Eliceiri, K. W. (2012). NIH Image to ImageJ: 25 years of image analysis. *Nature Methods*, 9(7), 671–675. <https://doi.org/10.1038/nmeth.2089>
- Steeffel, C. I., Appelo, C. A. J., Arora, B., Jacques, D., Kalbacher, T., Kolditz, O., Lagneau, V., Lichtner, P. C., Mayer, K. U., Meeussen, J. C. L., Molins, S., Moulton, D., Shao, H., Šimůnek, J., Spycher, N., Yabusaki, S. B., & Yeh, G. T. (2015). Reactive transport codes for subsurface environmental simulation. *Computational Geosciences*, 19(3), 445–478. <https://doi.org/10.1007/s10596-014-9443-x>
- Steeffel, C. I., DePaolo, D., & Lichtner, P. (2005). Reactive transport modeling: An essential tool and a new research approach for the Earth sciences. *Earth and Planetary Science Letters*, 240(3–4), 539–558. <https://doi.org/10.1016/j.epsl.2005.09.017>
- Su, D., Mayer, K. U., & MacQuarrie, K. T. B. (2021). MIN3P-HPC: A high-performance unstructured grid code for subsurface flow and reactive transport simulation. *Mathematical Geosciences*, 53(4), 517–550. <https://doi.org/10.1007/s11004-020-09898-7>
- Tötze, C., Kardjilov, N., Hilger, A., Rudolph-Mohr, N., Manke, I., & Oswald, S. E. (2021). Three-dimensional in vivo analysis of water uptake and translocation in maize roots by fast neutron tomography. *Scientific Reports*, 11(1), 10578. <https://doi.org/10.1038/s41598-021-90062-4>
- Tracy, S. R., Daly, K. R., Sturrock, C. J., Crout, N. M. J., Mooney, S. J., & Roose, T. (2015). Three-dimensional quantification of soil hydraulic properties using X-ray Computed Tomography and image-based modeling. *Water Resources Research*, 51(2), 1006–1022. <https://doi.org/10.1002/2014WR016020>
- Uteau, D., Pagenkemper, S. K., Peth, S., & Horn, R. (2013). Root and time dependent soil structure formation and its influence on gas transport in the subsoil. *Soil and Tillage Research*, 132, 69–76. <https://doi.org/10.1016/j.still.2013.05.001>
- van Genuchten, M. T. (1980). A closed-form equation for predicting the hydraulic conductivity of unsaturated soils. *Soil Science Society of America Journal*, 44(5), 892–898. <https://doi.org/10.2136/sssaj1980.03615995004400050002x>
- Vereecken, H., Schnepf, A., Hopmans, J. W., Javaux, M., Or, D., Roose, T., Vanderborght, J., Young, M. H., Amelung, W., Aitkenhead, M., Allison, S. D., Assouline, S., Baveye, P., Berli, M., Brüggemann, N., Finke, P., Flury, M., Gaiser, T., Govers, G., ... Young, I. M. (2016). Modeling soil processes: Review, key challenges, and new perspectives. *Vadose Zone Journal*, 15(5), vzj2015.09.0131. <https://doi.org/10.2136/vzj2015.09.0131>
- Wise, D. L., & Houghton, G. (1966). The diffusion coefficients of ten slightly soluble gases in water at 10–60°C. *Chemical Engineering Science*, 21(11), 999–1010. [https://doi.org/10.1016/0009-2509\(66\)85096-0](https://doi.org/10.1016/0009-2509(66)85096-0)
- Ye, Y., Chen, Y. F., Hu, R., & Yang, Z. (2021). Scaling relationships between van Genuchten model parameters and hydraulic conductivity. *IOP Conference Series: Earth and Environmental Science*, 861(7), 0–8. <https://doi.org/10.1088/1755-1315/861/7/072076>
- Zarebanadkouki, M., Fink, T., Benard, P., & Banfield, C. C. (2019). Mucilage facilitates nutrient diffusion in the drying rhizosphere. *Vadose Zone Journal*, 18(1), 1–13. <https://doi.org/10.2136/vzj2019.02.0021>
- Zarebanadkouki, M., Kim, Y. X., & Carminati, A. (2013). Where do roots take up water? Neutron radiography of water flow into the roots of transpiring plants growing in soil. *New Phytologist*, 199(4), 1034–1044. <https://doi.org/10.1111/nph.12330>
- Zhang, Y., & Schaap, M. G. (2017). Weighted recalibration of the Rosetta pedotransfer model with improved estimates of hydraulic parameter distributions and summary statistics (Rosetta3). *Journal of Hydrology*, 547, 39–53. <https://doi.org/10.1016/j.jhydrol.2017.01.004>

SUPPORTING INFORMATION

Additional supporting information can be found online in the Supporting Information section at the end of this article.

How to cite this article: Bereswill, S., Gatz-Miller, H., Su, D., Tötze, C., Kardjilov, N., Oswald, S. E., & Mayer, K. U. (2023). Coupling non-invasive imaging and reactive transport modeling to investigate water and oxygen dynamics in the root zone. *Vadose Zone Journal*, 22, e20268. <https://doi.org/10.1002/vzj2.20268>